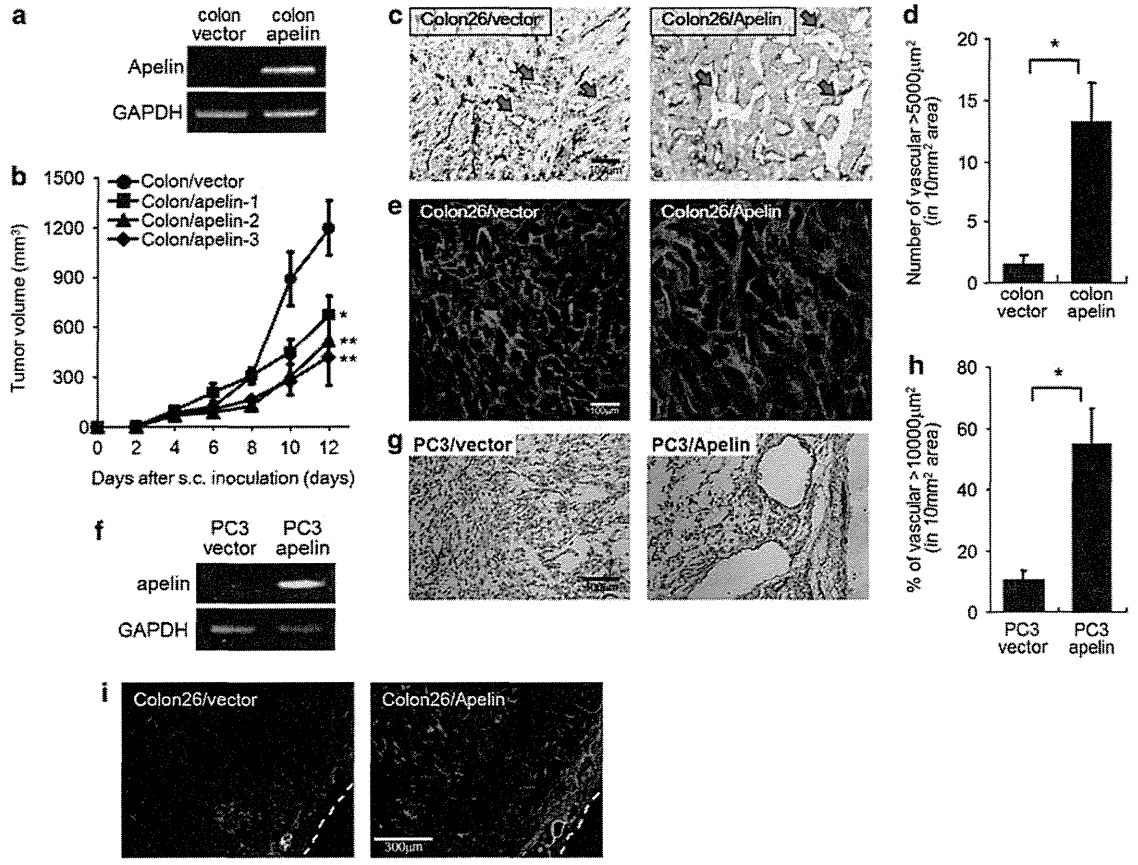

Figure 2 Apelin induces enlargement of blood vessels in tumors and inhibits tumor growth. (**a**) Reverse transcription–PCR (RT–PCR) analysis of apelin expression in colon26 tumor cells. GAPDH was used as a positive control. (**b**) The growth curves of control and apelin-overexpressing colon26 tumors implanted in the dorsa of BALB/c mice ($n = 10$ mice per group). $^*P < 0.05$; $^{**}P < 0.01$ (comparison with colon/vector tumor). (**c**) Immunohistochemical staining of sections from tumors generated by colon26 cells and colon26 cells transduced with apelin. Blood vessels were stained by an anti-CD31 mAb (brown). The arrows indicate typical vessels. Scale bar, 100 μm. (**d**) The number of enlarged blood vessels having a $> 5 \times 10^3$ μm² luminal cavity per 10-mm² area was quantitatively evaluated in each tumor section. $^*P < 0.001$. (**e**) Confocal imaging of 50-μm sections from tumors generated from colon26 cells or colon26 cells transduced with apelin. Sections were stained by an anti-CD31 mAb. (**f**) RT–PCR analysis of apelin expression in PC3 tumor cells. GAPDH was used as a positive control. (**g**) Immunohistochemical staining of sections from tumors generated from PC3 cells or PC3 cells transduced with apelin. Sections were stained by an anti-CD31 mAb (brown). Scale bar, 100 μm. (**h**) The number of enlarged blood vessels having a $> 10^4$ μm² luminal cavity per 10-mm² area was quantitatively evaluated in each tumor section. $^*P < 0.001$. (**i**) Immunohistochemical staining of sections from control colon26 tumors or apelin-overexpressing colon26 tumors using an anti-CD31 antibody (green) and an anti-α-smooth muscle actin antibody (red). Scale bar, 300 μm.

effector cell-mediated cancer immunotherapy, combined with vascular normalization, would demonstrate more significant antitumor effects than either treatment alone.

iNKT cells are a very small cell population in the peripheral blood before stimulation with αGalCer, a specific glycolipid antigen (Kawano *et al.*, 1997; Brossay *et al.*, 1998; Spada *et al.*, 1998). After activation, the iNKT cell population significantly expands and exerts strong antitumor activity against various malignant tumors both *in vivo* and *in vitro* (Kawano *et al.*, 1999; Shin *et al.*, 2001; Seino *et al.*, 2005). Therefore, we investigated the synergistic effects between vascular normalization with apelin and immunotherapy with αGalCer-pulsed DCs whose antitumor response had already reported in mice and humans (Nieda *et al.*, 2004; Kunii *et al.*, 2009; Motohashi *et al.*, 2009).

Prepared αGalCer-pulsed or vehicle-pulsed mature bone marrow (BM)-derived DCs (BMDCs) were analyzed by flow cytometry after 8 days of culture. Both groups of BMDCs highly expressed CD11c (83%) and major histocompatibility complex (MHC) class-II (about 95%); moreover, the expression levels of CD86 and CD80 were also high (60–90%) (Figure 4a). These cells were injected into mice on day 0 and then the number of peripheral iNKT cells was monitored. The iNKT cell populations were significantly elevated on day 4 in mice injected with αGalCer-pulsed BMDCs (Figure 4b). Alternately, peripheral iNKT cell numbers remained at low levels in mice injected with vehicle-pulsed DCs. Therefore, we used both sets of DCs for antitumor immunotherapy experiments.

Enhancement of antitumor effects by combination of apelin stimulation and DC treatment

To evaluate the synergistic effect of apelin-mediated normalization of the tumor vasculature and immu-

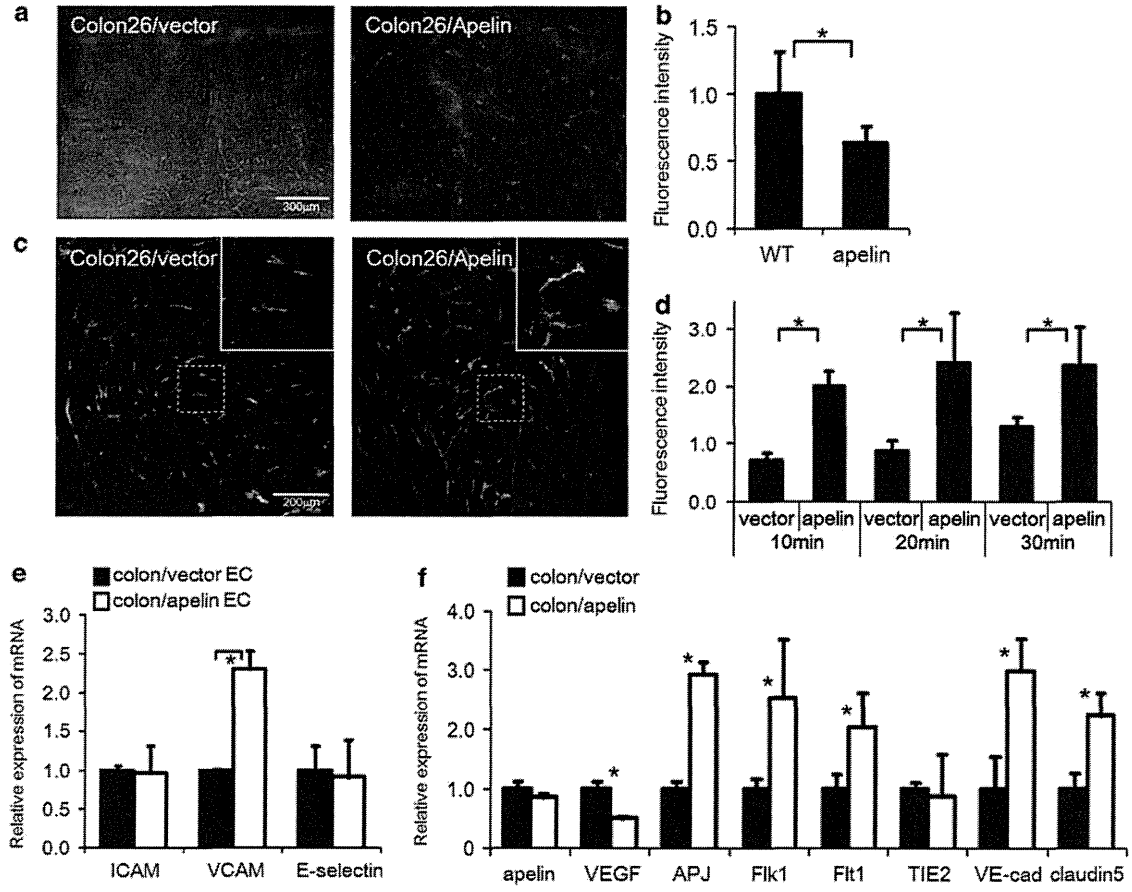

Figure 3 Apelin induces the formation of functional, non-leaky, mature vessels. (**a**) Colon26 control and apelin-overexpressing tumors were stained for CD31 (red) and hypoxia (HypoxyProbe, green). Scale bar, 100 μm. (**b**) The hypoxic region within the vascularized tumor was quantified by the fluorescence intensity in HypoxyProbe staining. $^*P<0.01$. (**c**) Microscopy images of fluorescein isothiocyanate–dextran angiography and the vasculature (CD31, red) on colon26 control and apelin-overexpressing tumors. Scale bar, 100 μm. (**d**) Time-course analysis of the fluorescence intensity of extravascular fluorescein isothiocyanate–dextran as a measure of vascular permeability. $^*P<0.01$. (**e**, **f**) Quantitative real-time RT–PCR analysis for cell adhesion molecules (**e**) or EC-related factors (**f**) using total RNA for CD31 + CD45− ECs isolated by cell sorting from colon26 control and apelin-overexpressing tumors. $^*P<0.01$.

notherapy with mature DCs, we analyzed the antitumor activity of the combination therapy. Development of the tumor vasculature was observed between 4 and 6 days after implantation of colon26 cells (Supplementary Figure 2). Therefore, after implantation of colon26/vector or colon26/apelin cells into the subcutaneous tissue of mice, mature DCs were administered by intravenous injection on day 4 and tumors were harvested on day 14 (Figure 5a). We observed antitumor effects, as described previously, in the apelin-expressing tumor or in vector-transduced colon26 tumors treated with αGalCer/DCs, but more remarkable antitumor effects were observed in mice that underwent both apelin transduction and DC treatment (Figures 5b–d). Growth of colon26/apelin tumors treated with αGalCer/DCs slowed when tumor volumes exceeded 100 mm^3 (Figure 5b). The tumor weight of colon26/apelin tumors treated with αGalCer/DCs was exceedingly small and comprised only about a fourth of the vehicle/DCs-treated, apelin-transduced colon26 tumors or αGalCer/DCs-treated, vector-transduced colon26 tumors (Figures 5c and d). These data suggest that the vascular normalization induced by apelin markedly improved the effects of immunotherapy.

To exclude the possibility that apelin activated the immune cells and enhanced their antitumor effect, we analyzed the expression of APJ in iNKT cells and DCs. Compared with tumor blood vascular ECs, APJ expression in iNKT cells and in each of the DCs was extremely low and almost undetectable, respectively (Figure 5e). Therefore, apelin is not likely to directly activate these cells.

Infiltration of iNKT cells into tumor tissues was promoted by apelin-induced vascular maturation

Finally, to confirm that the antitumor effect observed in the colon26/apelin tumors treated with αGalCer/DCs was actually caused by iNKT cell infiltration into tumor tissue or activation induced by the DCs, we analyzed tumor tissues, which were harvested 14 days after tumor cell inoculation. We observed higher levels of NKp46 + cell infiltration in αGalCer/DC-treated colon26/apelin tumors as compared with colon/vector tumors and

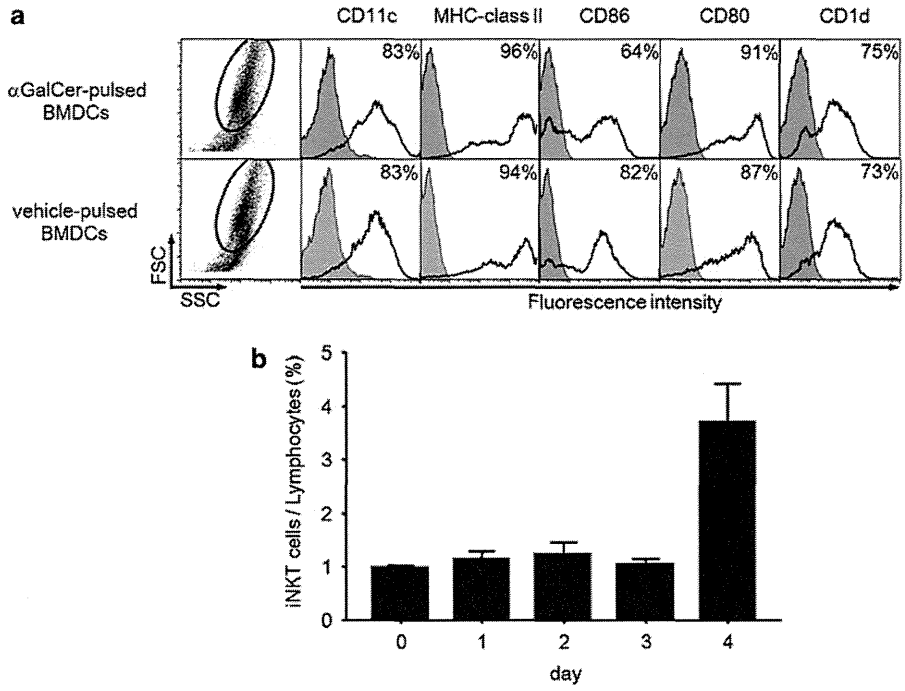

Figure 4 Functional analysis of αGalCer-pulsed mature BMDCs. (**a**) Flow-cytometric analysis of αGalCer- or vehicle-pulsed mature BMDCs. The expression levels of CD11c, human leukocyte antigen class-II, CD86, CD80 and CD1d were assessed at the time of administration. Thin lines: background staining with an isotype-matched control; bold line: staining profiles of the indicated molecules. (**b**) The percentage of peripheral blood iNKT cells (TCR-β + αGalCer-CD1d-tetramer + cells) after injection of αGalCer-pulsed mature BMDCs (6×10^5 cells) was assessed by flow-cytometric analysis.

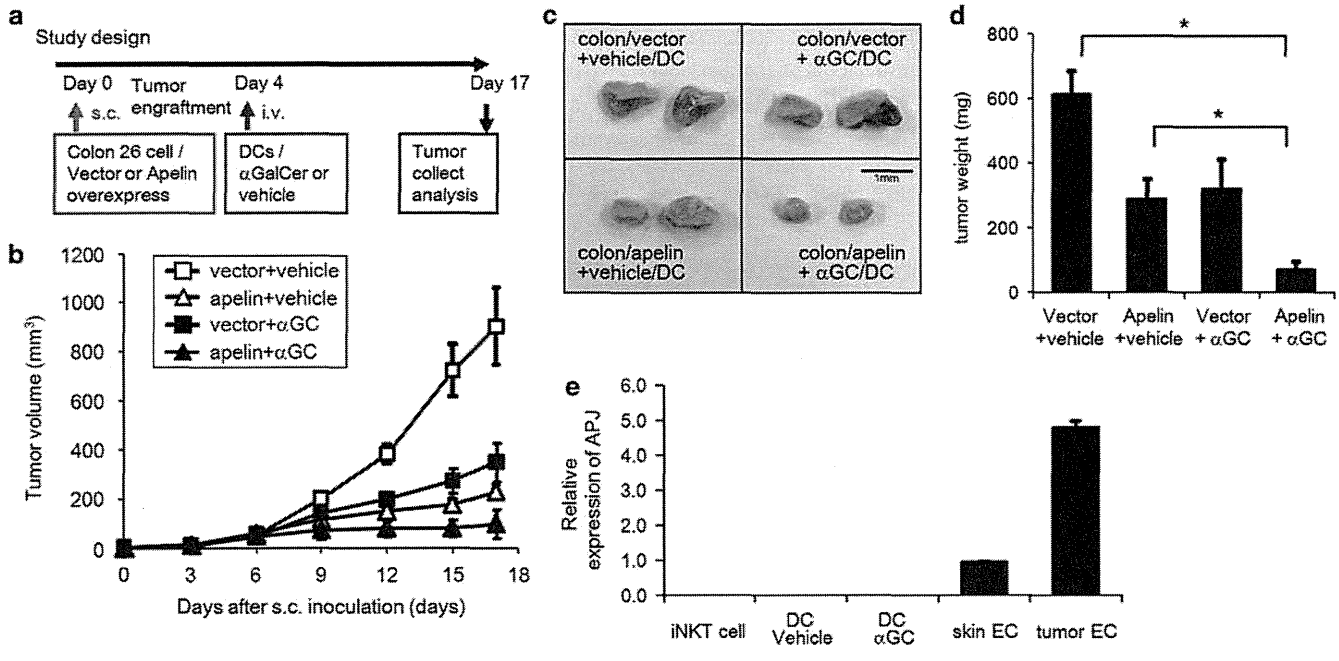

Figure 5 Enhancement of the antitumor effect by combination of apelin stimulation and DC treatment. (**a**) A schematic diagram of the experimental protocol of tumor isograft and DC treatment assays. (**b**) Growth curves of control and apelin-overexpressing colon26 tumors implanted in the dorsa of BALB/c mice treated with control vehicle-pulsed DCs or αGalCer-pulsed DCs ($n = 10$ mice per group). (**c**) Representative pictures of tumors collected 15 days after subcutaneous inoculation. Scale bar, 1 mm. (**d**) Tumor volume was determined on day 15 after subcutaneous inoculation of each tumor. $^*P < 0.01$. (**e**) Quantitative real-time RT–PCR analysis of APJ mRNA in iNKT cells and DCs. The results are shown as fold increase in comparison with the basal levels of normal ECs.

untreated tumors (Figure 6a). Consistent with this result, flow-cytometric analysis of αGalCer/DCs-treated colon/apelin tumors showed significant augmentation of iNKT cells (TCR-β + αGalCer-CD1d-tetramer +) in tumor tissues as compared with those in the untreated tumors (Figures 6b and c).

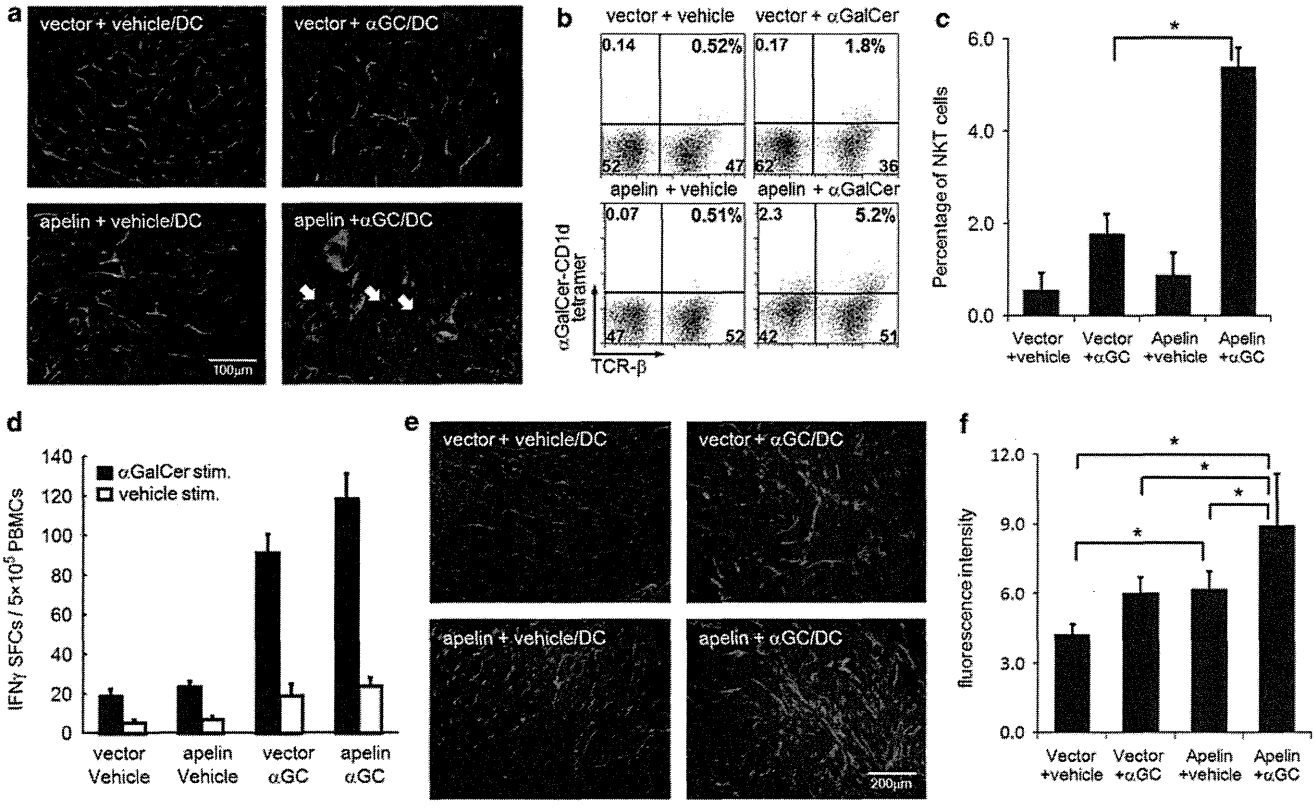

Figure 6 Infiltration of iNKT cells into tumor tissues was promoted by apelin-induced vascular maturation. (**a**) Immunohistochemical staining of sections from control and apelin-overexpressing colon26 tumors treated with control vehicle-pulsed DCs or αGalCer-pulsed DCs. Sections were stained by using anti-NKp46 (red) and anti-CD31 antibodies (green). Scale bar, 100 μm. (**b**) Flow-cytometric analysis of tumor-infiltrating CD45-positive lymphocytes. Cells were stained by a αGalCer-loaded CD1d tetramer and an anti-TCR-β antibody. (**c**) Quantitative evaluation of the percentage of iNKT cells (αGalCer-CD1d-tetramer + TCR-β + CD45 + iNKT cells/CD45 + lymphocytes) in tumor-infiltrating lymphocytes with s.d. $^*P<0.01$. (**d**) The mean number of IFNγ spot-forming cells with s.d., determined by ELISpot assay. A total of 5×10^5 peripheral blood mononuclear cells were stimulated for 16 h with αGalCer or vehicle *in vitro*. The mean numbers of IFN-γ spots were determined from triplicate cultures. (**e**) Apoptosis of tumor cells was detected by the TUNEL method (green) and blood vessels were stained with an anti-CD31 antibody (red). Scale bar, 200 μm. (**f**) Quantification of apoptosis in tumor sections by measurement of fluorescence intensity of TUNEL-positive cells. $^*P<0.01$.

IFN-γ production in response to αGalCer antigenic stimulation was increased in peripheral blood cells of mice treated with αGalCer/DCs (Figure 6d). Moreover, many apoptotic tumor cells were observed in αGalCer/DC-treated colon26/apelin tumors (Figures 6e and f). These results suggest that the potent antitumor effects observed in αGalCer/DC-treated colon26/apelin tumors was caused by enhanced infiltration of iNKT cells in the center of the tumor tissue, thus inducing apoptotic tumor cell death.

Discussion

We found that expression of APJ (the apelin receptor) was significantly increased in tumor blood vessels and apelin simulation induced enlargement of the caliber of tumor vessels. Enlargement of tumor vessels by apelin also led to functional maturation and normalization, including suppression of vascular permeability and improvement of oxygen supply to the central tumor.

Normalization of the tumor vasculature induced by VEGF-neutralizing antibodies has been reported to suppress tumor growth (Kim *et al.*, 1993). In our study, apelin-induced vascular maturation also demonstrated an antitumor growth effect. One of the major therapeutic benefits of tumor vascular normalization is enhancement of the effects of conventional cancer therapy such as chemotherapy, radiotherapy and immunotherapy. In our present study, we used a combination of immunotherapy with DC treatment with vascular normalization therapy due to apelin expression and obtained remarkable antitumor effects. These therapeutic effects resulted from induction of tumor cell apoptosis by effective infiltration of activated iNKT cells.

Several researchers have reported that apelin is relevant to blood vessel formation not only under physiological conditions, but also in a neoplastic context (Seaman *et al.*, 2007; Sorli *et al.*, 2007). Consistent with these results, we found that apelin expression was observed in vascular ECs of colon26 tumors and LLC tumors. In addition, we revealed that APJ expression was also upregulated in these tumor ECs. Our previous

report showed that APJ expression was induced by VEGF stimulation of ECs of blood vessels where angiogenesis is taking place (Kidoya *et al.*, 2008).We predict that APJ expression in tumor blood vessels is also regulated by the same mechanism, because angiogenesis is frequently observed in tumor tissues. Of interest, APJ-expressing angiogenic ECs are almost imperceptible in healthy adults. Although apelin has been reported to act on heart contractility and blood pressure regulation, apelin-deficient and apelin-overexpressing mice show normal growth after birth (Kidoya *et al.*, 2008, 2010). Therefore, anti-angiogenesis drugs targeting apelin would be expected to have fewer side effects than other anti-angiogenic agents targeting more ubiquitously expressed molecules such as VEGF.

We previously reported that apelin regulates the lumen size of the blood vessels of embryos during the vascular maturation process. In this report, we found that the tumor vasculature is also regulated by apelin stimulation. Blood vessels in tumors are functionally immature and characteristically leaky in nature (Bergers and Benjamin, 2003). From analysis of blood vessels in the skin of apelin-overexpressing mice, it was apparent that apelin can enhance vascular stability and suppress vascular permeability (Kidoya *et al.*, 2010). In the tumor vessels examined in our present study, we found that apelin improved stability and induced normalization by upregulating the expression of adhesion molecules in ECs.

Tumor blood vessels are structurally and functionally abnormal, and these abnormalities impair the tumor oxygen supply (Padera *et al.*, 2004). The hypoxic microenvironment formed in this manner induces genetic instability and leads to further alterations in malignant cells (Bottaro and Liotta, 2003). The vascular normalization induced by a VEGF-neutralizing antibody can alleviate the hypoxic condition of the tumor microenvironment and suppress malignant transformation. Apelin stimulation also improved the function of tumor blood vessels and alleviated the hypoxia. We attributed the growth suppression of the apelin-expressing tumors observed in this study to this effect. It is possible that tumor vessels normalized by apelin enhance the delivery of nutrients to tumor cells. However, this vascular normalization might also induce an antitumor effect by immunocyte infiltration, because the concentration of apoptotic tumor cells was increased in the colon/apelin + vehicle group as compared with the colon/vector + vehicle group, as shown in Figure 6f.

Contrary to our results, it has been reported that apelin induces tumor angiogenesis and promotes tumor growth (Sorli *et al.*, 2007). This difference might depend on the particular apelin–APJ signaling pathway that has been activated, such as the angiopietin1–Tie2 signaling pathway (Fukuhara *et al.*, 2008). The apelin–APJ system activates the Akt and ERK (extracellular-signal regulated kinase) signaling pathways, which might be involved in vascular stabilization and pro-angiogenesis, respectively. Therefore, apelin may have a beneficial effect in cancer treatment, if it can be predicted before treatment in individual cases that apelin induces normalization of the tumor vasculature.

Current immunotherapy for human solid cancers can be classified into the following categories (Rosenberg *et al.*, 2008): one is non-specific immunomodulation, such as interleukin-2 therapy for renal cancer or metastatic melanoma (Rosenberg *et al.*, 1989). Another is use of a cancer vaccine containing tumor peptides or DCs (Steinman and Banchereau, 2007) that activates the patient's immunity against their cancer. The last category is adoptive cell transfer, in which *in vitro* expanded autologous antitumor effector cells are administered to the patient (Rosenberg *et al.*, 2008). In all of these treatments, effector cell delivery to the tumor site is indispensable, and therefore, improvements in delivery would increase the therapeutic effects of all of these approaches. In this study, we used the DC therapy targeted to iNKT cells because tumor-infiltrating cells can be specifically evaluated. There are few iNKT cells at the tumor site before stimulation, and significant expansions of iNKT cells were observed after activation with the unique antigen. Based on these findings, it was strongly expected that combination with vascular normalization therapy would also improve the efficacy of the other immunotherapy such as tumor antigen-specific T-cell therapy. Therefore, as a follow-up study, we are preparing to examine combination treatment by adoptive cell transfer using engineered T lymphocytes (June *et al.*, 2009), and the difference in infiltration into the tumor site between iNKT cells and conventional T cells will be assessed.

Induction of vascular normalization leads to enhancement of the efficacy of conventional therapies (Willett *et al.*, 2006). Here we have demonstrated that combination therapy using vascular maturation induced by apelin and immune therapy with administration of antigen-loaded DCs remarkably suppressed the growth of colon26 tumors. This antitumor effect was attributed to dramatic infiltration of DC-activated iNKT cells and subsequent induction of apoptosis in the tumor cells. It was recently reported that inhibition of angiogenesis lead to normalized endothelial adhesion molecule levels and improves tumor growth inhibition by promoting leukocyte extravasation (Dings *et al.*, 2011). Upregulation of VCAM1 expression was also induced in the endothelium of apelin-expressing tumor, and it would promote iNKT cell infiltration. Tumor vascular normalization induced by apelin therefore appears to augment immunotherapy as well as chemotherapy and radiotherapy.

In summary, our data suggest that vascular normalization induced by apelin can enhance the effect of immunotherapy by promoting immune cell recruitment. Many angiogenic factors have been identified, and their functions have been described, and many of these factors have been or are being targeted as new cancer therapy approaches. Compared with these angiogenic molecules, apelin has a unique function in that it regulates blood vessel maturation, but has limited functions with regard to induction of angiogenesis. In addition, apelin-targeting agents would have fewer side effects, because expression of the apelin receptor, APJ, is confined to newly formed blood vessels such as tumor

vessels. Induction of tumor vascular normalization by recombinant apelin administration is difficult because the apelin peptide is unstable. For these reasons, the design of drugs that target the apelin–APJ system, such as more stable and potent APJ receptor agonist, is expected to provide novel agents that by regulating the tumor vasculature will introduce an effective new cancer treatment.

Materials and methods

Mice
C57BL/6 mice, KSN nude mice and BALB/c mice at 8 weeks of age were purchased from Japan SLC (Shizuoka, Japan) and were used between 8 and 12 weeks of age. The animals were housed in environmentally controlled rooms of the animal experimentation facility at Osaka University. All experiments were performed in compliance with the laws and institutional guidelines of Osaka University.

Cells
Cell lines, including colon26, PC3 and LLC, were purchased from RIKEN cell bank (Tsukuba, Japan). The culture medium used was RPMI-1640 containing 10% fetal calf serum, 50 μM 2-mercaptoethanol, 2 mM glutamine and 10 mM HEPES buffer. DCs were grown from bone marrow progenitors in culture medium supplemented with 20 ng/ml recombinant murine granulocyte–macrophage colony-stimulating factor (eBioscience, San Diego, CA, USA) (Fujii *et al.*, 2002). On day 6, αGalCer (100 ng/ml; Kyowa Hakko, Gunma, Japan) was added to immature BMDCs for 40 h. To induce maturation of the DCs, 100 ng/ml lipopolysaccharide (Wako, Osaka, Japan) was added on day 7 for 16 h. Mature αGalCer-pulsed DCs were collected on day 8.

Tissue preparation, immunohistochemistry and flow cytometry
Tissue fixation and staining of sections with antibodies were performed as described previously (Takakura *et al.*, 2000). An anti-CD31 monoclonal antibody (mAb) (BD Biosciences, San Diego, CA, USA), anti-α-smooth muscle actin mAb (Dako, Glostrup, Denmark), anti-apelin mAb (4G5) (Kawamata *et al.*, 2001), anti-APJ polyclonal Ab (Kidoya *et al.*, 2008) and an anti-NKp46 mAb (R&D Systems, Minneapolis, MN, USA) were used for staining. TUNEL (TdT-mediated dNTP nick end labeling) assays were performed using the ApopTag Plus kit (Millipore, Billerica, MA, USA). Sections were observed by conventional microscopy (DM5500 B; Leica, Wetzlar, Germany) or confocal microscopy (TCS/SP5; Leica), and images were acquired with a digital camera (DFC500; Leica). In all assays, an isotype-matched control Ig was used as negative control and it was confirmed that the positive signals were not derived from nonspecific background. Images were processed using the Photoshop CS2 software (Adobe Systems, San Jose, CA, USA). Flow-cytometric analysis was performed as described previously (Yamada and Takakura, 2006). Fluorescence-labeled anti-CD45, anti-CD31, anti-CD86, anti-MHC class-II, anti-TCR-β, anti-CD1d, anti-CD80, anti-CD11c antibody (BD Biosciences) and CD1d tetramer antibodies (Proimmune, Oxford, UK) were used. Stained cells were analyzed with a FACSCalibur (BD Biosciences), by using the FlowJo software (TreeStar, Ashland, OR, USA), and sorted by using a JSAN flow cytometer (Bay Bioscience, Kobe, Japan). Dead cells were excluded from propidium iodide staining or analyses using the two-dimensional profile of the forward versus side scatter.

Real-time PCR analysis
Total RNA was extracted by using the RNeasy plus kit (Qiagen, Hilden, Germany) and reverse-transcribed into cDNA using the ExScript RT-PCR kit (Takara, Otsu, Japan). The primer pairs used for analysis are listed in Supplementary Table 1. Real-time PCR analysis was performed by using Platinum SYBR-Green SuperMix-UDG (Invitrogen, Carlsbad, CA, USA). The levels of PCR products were monitored with an Mx3000P QPCR system (Agilent, Santa Clara, CA, USA). Baseline and threshold were adjusted according to the manufacturer's instructions. The relative abundance of transcripts was normalized to the constitutive expression level of glyceraldehyde-3-phosphate dehydrogenase (GAPDH) RNA.

Tumor growth assay
The mouse *Apelin* gene was cloned into the pCAGSIH expression vector (Kidoya *et al.*, 2008). Colon26 cells and PC3 cells were stably transfected by using the Lipofectamine Plus reagent (Invitrogen) and clones of cells showing stable transfection were obtained by antibiotic resistance selection using G418 (Gibco, Grand Island, NY, USA) and hygromycin-B (Sigma, St Louis, MO, USA). The stably transfected colon26 clones (1×10^6 cells), PC3 clones (1×10^7 cells) or LLC cells (3×10^6 cells) were inoculated subcutaneously into 6- to 8-week-old BALB/c mice, nude mice or C57BL/6 mice, respectively, and tumors were dissected at 12–15 days after implantation. DCs (6×10^5 cells) were administered by intravenous injection 4 days after tumor implantation. To measure hypoxia in tumor tissues, HypoxyProbe-1 (Millipore; 60 mg/kg) was injected intraperitoneally 1 h before killing. Tumors sections were stained using an anti-HypoxyProbe antibody. To evaluate macromolecule infiltration, mice were intravenously injected with fluorescein isothiocyanate-conjugated dextran (500 μg; Vector Laboratories, Burlingame, CA, USA) and dextran was circulated for 10–30 min.

ELISpot assay
IFN-γ-producing cells were analyzed with a mouse IFN-γ ELISpot kit (Mabtech AB, Stockholm, Sweden). Peripheral blood mononuclear cells (5×10^5 per well, 96-well plates) were stimulated by addition of 100 ng/ml αGalCer or vehicle. Concanavalin-A was used as a positive control. IFN-γ spot-forming cells were quantified objectively by using an ImmunoScan computer system and the ImmunoSpot software program (CTL, Cleveland, OH, USA).

Statistical analysis
All data are presented as the means ± s.d. For statistical analysis, the statcel2 software package (OMS, Saitama, Japan) was used, with analysis of variance performed on all data, followed by the Tukey–Kramer multiple comparison test. When only two groups were compared, a two-sided Student's *t*-test was used.

Conflict of interest

The authors declare no conflict of interest.

Acknowledgements

We thank Ms C Takeshita, Ms K Fukuhara and Ms N Fujimoto for technical assistance. *Financial support*: This work

was supported by Grant-in-Aid for Research Activity Start-up (KAKENHI 21890124) from the Japan Society for the Promotion of Science (JSPS) and Research; a grant from the Ministry of Education, Culture, Sports, Science and Technology (MEXT) of Japan; and the YASUDA Medical Foundation.

References

Bergers G, Benjamin LE. (2003). Tumorigenesis and the angiogenic switch. *Nat Rev Cancer* **3**: 401–410.

Bottaro DP, Liotta LA. (2003). Cancer: out of air is not out of action. *Nature* **423**: 593–595.

Brossay L, Chioda M, Burdin N, Koezuka Y, Casorati G, Dellabona P *et al.* (1998). CD1d-mediated recognition of an alpha-galactosylceramide by natural killer T cells is highly conserved through mammalian evolution. *J Exp Med* **188**: 1521–1528.

Cox CM, D'Agostino SL, Miller MK, Heimark RL, Krieg PA. (2006). Apelin, the ligand for the endothelial G-protein-coupled receptor, APJ, is a potent angiogenic factor required for normal vascular development of the frog embryo. *Dev Biol* **296**: 177–189.

Dai T, Ramirez-Correa G, Gao WD. (2006). Apelin increases contractility in failing cardiac muscle. *Eur J Pharmacol* **553**: 222–228.

Dickson PV, Hamner JB, Sims TL, Fraga CH, Ng CY, Rajasekeran S *et al.* (2007). Bevacizumab-induced transient remodeling of the vasculature in neuroblastoma xenografts results in improved delivery and efficacy of systemically administered chemotherapy. *Clin Cancer Res* **13**: 3942–3950.

Dings RP, Vang KB, Castermans K, Popescu F, Zhang Y, Oude Egbrink MG *et al.* (2011). Enhancement of T-cell-mediated antitumor response: angiostatic adjuvant to immunotherapy against cancer. *Clin Cancer Res* **17**: 3134–3145.

Eyries M, Siegfried G, Ciumas M, Montagne K, Agrapart M, Lebrin F *et al.* (2008). Hypoxia-induced apelin expression regulates endothelial cell proliferation and regenerative angiogenesis. *Circ Res* **103**: 432–440.

Fujii S, Shimizu K, Kronenberg M, Steinman RM. (2002). Prolonged IFN-gamma-producing NKT response induced with alpha-galactosylceramide-loaded DCs. *Nat Immunol* **3**: 867–874.

Fukuhara S, Sako K, Minami T, Noda K, Kim HZ, Kodama T *et al.* (2008). Differential function of Tie2 at cell–cell contacts and cell-substratum contacts regulated by angiopoietin-1. *Nat Cell Biol* **10**: 513–526.

Gasparini G, Longo R, Toi M, Ferrara N. (2005). Angiogenic inhibitors: a new therapeutic strategy in oncology. *Nat Clin Pract Oncol* **2**: 562–577.

Gerber HP, Ferrara N. (2005). Pharmacology and pharmacodynamics of bevacizumab as monotherapy or in combination with cytotoxic therapy in preclinical studies. *Cancer Res* **65**: 671–680.

Gerhardt H, Betsholtz C. (2003). Endothelial-pericyte interactions in angiogenesis. *Cell Tissue Res* **314**: 15–23.

Heath VL, Bicknell R. (2009). Anticancer strategies involving the vasculature. *Nat Rev Clin Oncol* **6**: 395–404.

Hurwitz H, Fehrenbacher L, Novotny W, Cartwright T, Hainsworth J, Heim W *et al.* (2004). Bevacizumab plus irinotecan, fluorouracil, and leucovorin for metastatic colorectal cancer. *N Engl J Med* **350**: 2335–2342.

Jain RK. (2005). Normalization of tumor vasculature: an emerging concept in antiangiogenic therapy. *Science* **307**: 58–62.

June CH, Blazar BR, Riley JL. (2009). Engineering lymphocyte subsets: tools, trials and tribulations. *Nat Rev Immunol* **9**: 704–716.

Kakimi K, Guidotti LG, Koezuka Y, Chisari FV. (2000). Natural killer T cell activation inhibits hepatitis B virus replication *in vivo*. *J Exp Med* **192**: 921–930.

Kälin RE, Kretz MP, Meyer AM, Kispert A, Heppner FL, Brändli AW. (2007). Paracrine and autocrine mechanisms of apelin signaling govern embryonic and tumor angiogenesis. *Dev Biol* **305**: 599–614.

Kasai A, Shintani N, Kato H, Matsuda S, Gomi F, Haba R *et al.* (2008). Retardation of retinal vascular development in apelin-deficient mice. *Arterioscler Thromb Vasc Biol* **28**: 1717–1722.

Kasai A, Shintani N, Oda M, Kakuda M, Hashimoto H, Matsuda T *et al.* (2004). Apelin is a novel angiogenic factor in retinal endothelial cells. *Biochem Biophys Res Commun* **325**: 395–400.

Kawamata Y, Habata Y, Fukusumi S, Hosoya M, Fujii R, Hinuma S *et al.* (2001). Molecular properties of apelin: tissue distribution and receptor binding. *Biochim Biophys Acta* **1538**: 162–171.

Kawano T, Cui J, Koezuka Y, Toura I, Kaneko Y, Motoki K *et al.* (1997). CD1d-restricted and TCR-mediated activation of valpha14 NKT cells by glycosylceramides. *Science* **278**: 1626–1629.

Kawano T, Nakayama T, Kamada N, Kaneko Y, Harada M, Ogura N *et al.* (1999). Antitumor cytotoxicity mediated by ligand-activated human V alpha24 NKT cells. *Cancer Res* **59**: 5102–5105.

Kidoya H, Naito H, Takakura N. (2010). Apelin induces enlarged and nonleaky blood vessels for functional recovery from ischemia. *Blood* **115**: 3166–3174.

Kidoya H, Ueno M, Yamada Y, Mochizuki N, Nakata M, Yano T *et al.* (2008). Spatial and temporal role of the apelin/APJ system in the caliber size regulation of blood vessels during angiogenesis. *EMBO J* **27**: 522–534.

Kim KJ, Li B, Winer J, Armanini M, Gillett N, Phillips HS *et al.* (1993). Inhibition of vascular endothelial growth factor-induced angiogenesis suppresses tumour growth *in vivo*. *Nature* **362**: 841–844.

Kunii N, Horiguchi S, Motohashi S, Yamamoto H, Ueno N, Yamamoto S *et al.* (2009). Combination therapy of *in vitro*-expanded natural killer T cells and alpha-galactosylceramide-pulsed antigen-presenting cells in patients with recurrent head and neck carcinoma. *Cancer Sci* **100**: 1092–1098.

Lago F, Dieguez C, Gomez-Reino J, Gualillo O. (2007). The emerging role of adipokines as mediators of inflammation and immune responses. *Cytokine Growth Factor Rev* **18**: 313–325.

Lambrecht NW, Yakubov I, Zer C, Sachs G. (2006). Transcriptomes of purified gastric ECL and parietal cells: identification of a novel pathway regulating acid secretion. *Physiol Genomics* **25**: 153–165.

Lohela M, Bry M, Tammela T, Alitalo K. (2009). VEGFs and receptors involved in angiogenesis versus lymphangiogenesis. *Curr Opin Cell Biol* **21**: 154–165.

Masri B, Morin N, Cornu M, Knibiehler B, Audigier Y. (2004). Apelin (65-77) activates p70 S6 kinase and is mitogenic for umbilical endothelial cells. *FASEB J* **18**: 1909–1911.

Motohashi S, Nagato K, Kunii N, Yamamoto H, Yamasaki K, Okita K *et al.* (2009). A phase I–II study of alpha-galactosylceramide-pulsed IL-2/GM-CSF-cultured peripheral blood mononuclear cells in patients with advanced and recurrent non-small cell lung cancer. *J Immunol* **182**: 2492–2501.

Nieda M, Nicol A, Koezuka Y, Kikuchi A, Lapteva N, Tanaka Y *et al.* (2001). TRAIL expression by activated human CD4(+)V alpha 24NKT cells induces *in vitro* and *in vivo* apoptosis of human acute myeloid leukemia cells. *Blood* **97**: 2067–2074.

Nieda M, Okai M, Tazbirkova A, Lin H, Yamaura A, Ide K *et al.* (2004). Therapeutic activation of Valpha24+Vbeta11+ NKT cells in human subjects results in highly coordinated secondary activation of acquired and innate immunity. *Blood* **103**: 383–389.

Padera TP, Stoll BR, Tooredman JB, Capen D, di Tomaso E, Jain RK. (2004). Pathology: cancer cells compress intratumour vessels. *Nature* **427**: 695.

Rosenberg SA, Lotze MT, Yang JC, Aebersold PM, Linehan WM, Seipp CA *et al.* (1989). Experience with the use of high-dose interleukin-2 in the treatment of 652 cancer patients. *Ann Surg* **210**: 474–484; discussion 484–475.

Rosenberg SA, Restifo NP, Yang JC, Morgan RA, Dudley ME. (2008). Adoptive cell transfer: a clinical path to effective cancer immunotherapy. *Nat Rev Cancer* **8**: 299–308.

Seaman S, Stevens J, Yang MY, Logsdon D, Graff-Cherry C, St Croix B. (2007). Genes that distinguish physiological and pathological angiogenesis. *Cancer Cell* **11**: 539–554.

Seino K, Fujii S, Harada M, Motohashi S, Nakayama T, Fujisawa T *et al.* (2005). Valpha14 NKT cell-mediated antitumor responses and their clinical application. *Springer Semin Immunopathol* **27**: 65–74.

Shin T, Nakayama T, Akutsu Y, Motohashi S, Shibata Y, Harada M *et al.* (2001). Inhibition of tumor metastasis by adoptive transfer of IL-12-activated Valpha14 NKT cells. *Int J Cancer* **91**: 523–528.

Singh AK, Wilson MT, Hong S, Olivares-Villagomez D, Du C, Stanic AK *et al.* (2001). Natural killer T cell activation protects mice against experimental autoimmune encephalomyelitis. *J Exp Med* **194**: 1801–1811.

Smyth MJ, Crowe NY, Pellicci DG, Kyparissoudis K, Kelly JM, Takeda K *et al.* (2002). Sequential production of interferon-gamma by NK1.1(+) T cells and natural killer cells is essential for the antimetastatic effect of alpha-galactosylceramide. *Blood* **99**: 1259–1266.

Sorhede Winzell M, Magnusson C, Ahren B. (2005). The apj receptor is expressed in pancreatic islets and its ligand, apelin, inhibits insulin secretion in mice. *Regul Pept* **131**: 12–17.

Sorli SC, Le Gonidec S, Knibiehler B, Audigier Y. (2007). Apelin is a potent activator of tumour neoangiogenesis. *Oncogene* **26**: 7692–7699.

Spada FM, Koezuka Y, Porcelli SA. (1998). CD1d-restricted recognition of synthetic glycolipid antigens by human natural killer T cells. *J Exp Med* **188**: 1529–1534.

Steinman RM, Banchereau J. (2007). Taking dendritic cells into medicine. *Nature* **449**: 419–426.

Takakura N, Watanabe T, Suenobu S, Yamada Y, Noda T, Ito Y *et al.* (2000). A role for hematopoietic stem cells in promoting angiogenesis. *Cell* **102**: 199–209.

Taniguchi M, Harada M, Kojo S, Nakayama T, Wakao H. (2003). The regulatory role of Valpha14 NKT cells in innate and acquired immune response. *Annu Rev Immunol* **21**: 483–513.

Tatemoto K, Hosoya M, Habata Y, Fujii R, Kakegawa T, Zou MX *et al.* (1998). Isolation and characterization of a novel endogenous peptide ligand for the human APJ receptor. *Biochem Biophys Res Commun* **251**: 471–476.

Willett CG, Kozin SV, Duda DG, di Tomaso E, Kozak KR, Boucher Y *et al.* (2006). Combined vascular endothelial growth factor-targeted therapy and radiotherapy for rectal cancer: theory and clinical practice. *Semin Oncol* **33**: S35–S40.

Yamada Y, Takakura N. (2006). Physiological pathway of differentiation of hematopoietic stem cell population into mural cells. *J Exp Med* **203**: 1055–1065.

Supplementary Information accompanies the paper on the Oncogene website (http://www.nature.com/onc)

nature medicine

Endothelial PI3K-C2α, a class II PI3K, has an essential role in angiogenesis and vascular barrier function

Kazuaki Yoshioka[1,13], Kotaro Yoshida[1,2,13], Hong Cui[1], Tomohiko Wakayama[3], Noriko Takuwa[1,4], Yasuo Okamoto[1], Wa Du[1], Xun Qi[1], Ken Asanuma[5], Kazushi Sugihara[6], Sho Aki[1], Hidekazu Miyazawa[1], Kuntal Biswas[1], Chisa Nagakura[1], Masaya Ueno[7], Shoichi Iseki[3], Robert J Schwartz[8], Hiroshi Okamoto[9], Takehiko Sasaki[5,10], Osamu Matsui[2], Masahide Asano[6], Ralf H Adams[11,12], Nobuyuki Takakura[7] & Yoh Takuwa[1]

The class II α-isoform of phosphatidylinositol 3-kinase (PI3K-C2α) is localized in endosomes, the *trans*-Golgi network and clathrin-coated vesicles; however, its functional role is not well understood. Global or endothelial-cell–specific deficiency of PI3K-C2α resulted in embryonic lethality caused by defects in sprouting angiogenesis and vascular maturation. PI3K-C2α knockdown in endothelial cells resulted in a decrease in the number of PI3-phosphate–enriched endosomes, impaired endosomal trafficking, defective delivery of VE-cadherin to endothelial cell junctions and defective junction assembly. PI3K-C2α knockdown also impaired endothelial cell signaling, including vascular endothelial growth factor receptor internalization and endosomal RhoA activation. Together, the effects of PI3K-C2α knockdown led to defective endothelial cell migration, proliferation, tube formation and barrier integrity. Endothelial PI3K-C2α deficiency *in vivo* suppressed postischemic and tumor angiogenesis and diminished vascular barrier function with a greatly augmented susceptibility to anaphylaxis and a higher incidence of dissecting aortic aneurysm formation in response to angiotensin II infusion. Thus, PI3K-C2α has a crucial role in vascular formation and barrier integrity and represents a new therapeutic target for vascular disease.

Formation of the vascular network by vasculogenesis and angiogenesis is essential for embryonic development, repair and remodeling of tissues in adults, and tumor growth. The angiogenic response to vascular endothelial growth factor (VEGF) and other factors begins with vascular leakage and dissolution of the subendothelial basement membrane, which is followed by the proliferation and migration of vascular endothelial cells[1,2]. Then, formation of intercellular junctions results in initial sprout formation from existing vessels. The newly formed endothelial tubes mature and become stabilized through their association with mural cells (smooth muscle cells (SMC) and pericytes)[3]. The tightness of the intercellular junctions, particularly adherens junctions composed of VE-cadherin and the associated proteins, controls vascular permeability[4,5]. Quiescent, stabilized vasculature with intact barrier integrity dominates in the healthy condition. In contrast, in pathological conditions such as tumors, the vasculature is immature and leaky. In the case of vascular insult such as that induced by excessive angiotensin II (Ang II) stimulation, increased vascular permeability is associated with leukocyte infiltration in the vascular wall and vascular disruption[6,7]. Therefore, stabilization of the vasculature and maintenance of vascular integrity is essential for vascular and tissue homeostasis[8,9].

PI3Ks comprise a family of enzymes that phosphorylate membrane inositol lipids at the 3′ position of the inositol ring. The lipid products of PI3Ks serve as important intracellular messengers by interacting with effector proteins, including protein kinases, guanine nucleotide exchangers for G proteins and actin cytoskeleton-regulating proteins. Through these actions, PI3Ks regulate a diverse array of cellular processes[10–12]. Three classes of PI3Ks exist. Class I PI3Ks, which are activated by tyrosine kinases and G protein–coupled receptors, consist of four catalytic subunits, p110α, p110β, p110γ and p110δ, and produce mainly phosphatidylinositol 3,4,5-trisphosphates (PtdIns(3,4,5)P_3). In endothelial cells, class I PI3Ks, in particular p110α, are indispensable for angiogenesis in the early embryo by regulating endothelial cell proliferation, migration and morphogenesis[13,14]. There is only one class III PI3K, Vps34, which generates PtdIns(3)P to regulate vesicular trafficking and autophagy[15]. In contrast to class I and III PI3Ks, the physiological functions of class II PI3Ks are not well understood. There are three members of the class II PI3K subfamily, which produce mainly PtdIns(3)P *in vivo*[16,17]: PI3K-C2α (C2α), PI3K-C2β (C2β) and PI3K-C2γ (C2γ). C2α is distinct from C2β, C2γ and other PI3K isoforms in that it has unique structural features, including a

[1]Department of Physiology, Kanazawa University School of Medicine, Kanazawa, Japan. [2]Department of Radiology, Kanazawa University School of Medicine, Kanazawa, Japan. [3]Department of Histology and Embryology, Kanazawa University School of Medicine, Kanazawa, Japan. [4]Department of Health and Medical Sciences, Ishikawa Prefectural Nursing University, Kahoku, Japan. [5]Department of Medical Biology, Akita University Graduate School of Medicine, Akita, Japan. [6]Division of Transgenic Animal Science, Advanced Science Research Center, Kanazawa University, Kanazawa, Japan. [7]Department of Signal Transduction, Research Institute for Microbial Diseases, Osaka University, Osaka, Japan. [8]Department of Biology and Biochemistry, University of Houston, Houston, Texas, USA. [9]Department of Medical Biochemistry, Tohoku University School of Medicine, Sendai, Japan. [10]Research Center for Biosignal, Akita University, Akita, Japan. [11]Max Planck Institute for Molecular Biomedicine, Department of Tissue Morphogenesis, Muenster, Germany. [12]University of Muenster, Faculty of Medicine, Muenster, Germany. [13]These authors contributed equally to this work. Correspondence should be addressed to Y.T. (ytakuwa@med.kanazawa-u.ac.jp).

Received 19 April; accepted 10 August; published online 16 September 2012; doi:10.1038/nm.2928

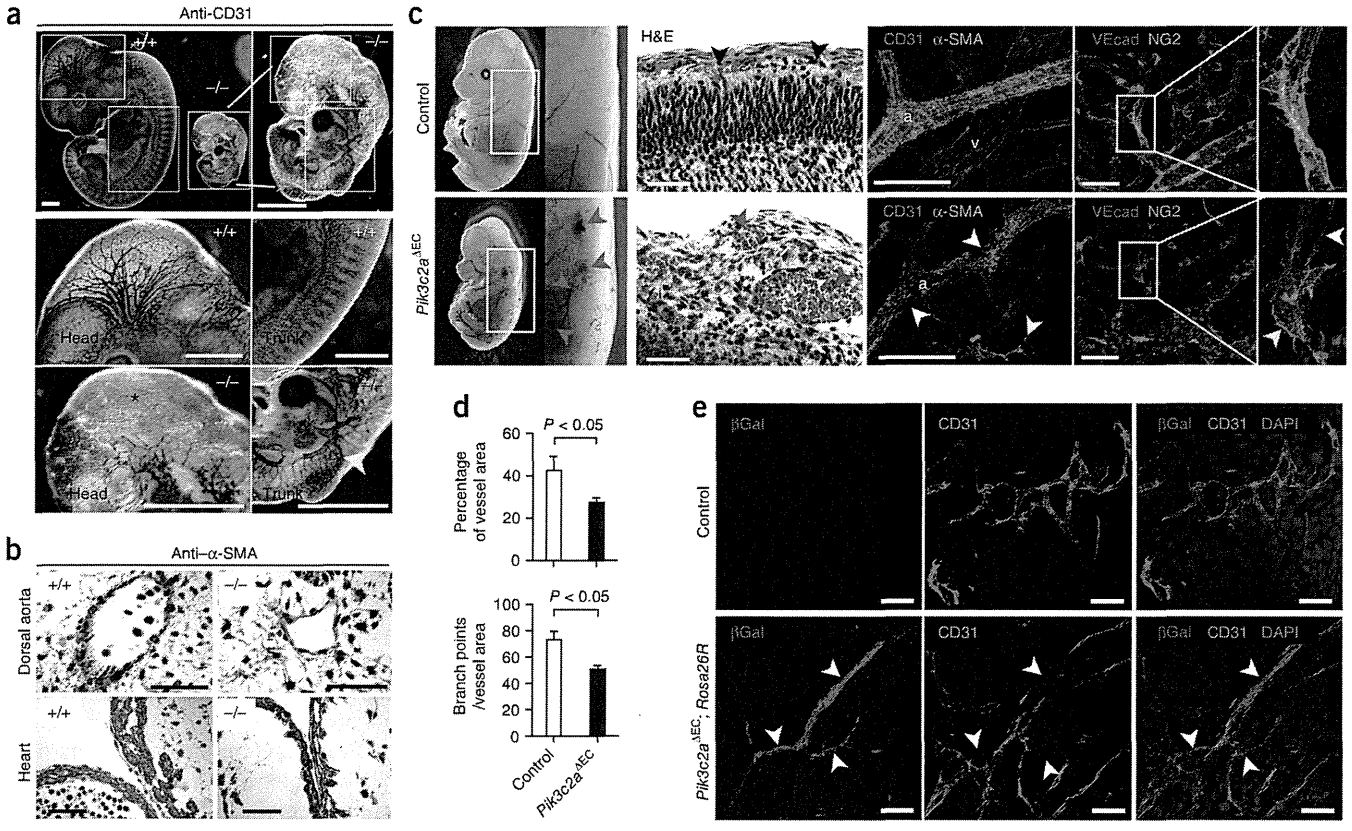

Figure 1 Endothelial C2α is necessary for developmental angiogenesis. (**a**) Whole-mount CD31-specific immunohistochemical staining of the vasculature in E11.5 wild-type (+/+) and global *Pik3c2a*$^{-/-}$ embryos. The magnified views show the brain (asterisk, bottom left), dorsal aorta (red arrowhead, bottom right) and intersomitic vessels (yellow arrowhead, bottom right) in *Pik3c2a*$^{-/-}$ embryos. Scale bars, 2 mm. (**b**) α-SMA–specific immunohistochemical staining in cross sections of dorsal aorta and heart from E11.5 wild-type and *Pik3c2a*$^{-/-}$ embryos. Scale bars, 100 μm. (**c**) Left and middle, gross views and H&E staining of skin sections of E15.5 wild-type and homozygous endothelial-cell–specific C2α-deletion mutant (*Pik3c2a*$^{\Delta EC}$) embryos (red arrowheads, dilated vessels and hemorrhage; black arrowheads, normal dermal vessels). Right, whole-mount double immunofluorescence staining of skin sections from E15.5 control and *Pik3c2a*$^{\Delta EC}$ embryos using CD31-specific (red) and α-SMA–specific (green), and VE-cadherin–specific (VEcad, red) and NG2-specific (green) staining. For CD31 and α-SMA staining, white and yellow arrowheads indicate SMC-uncovered areas and dettached SMCs, respectively; for VE-cadherin and NG2 staining, yellow and white arrowheads indicate loosely attached and detached pericytes, respectively. a, arteriole; v, venule. Scale bars, 100 μm. (**d**) Quantification of the CD31-positive vessel area per microscopic field (%) and branch points per vessel area in the skin. $n = 6$ mice per group. Data shown are the means ± s.e.m., and statistical significance was analyzed by Mann-Whitney *U* test. (**e**) CD31-specific and β-galactosidase (βGal)-specific double immunofluorescent staining of brain sections from E15.5 control (*Pik3c2a*$^{flox/flox}$; *Rosa26R*) and endothelial-cell–specific C2α-deleted (*Pik3c2a*$^{\Delta EC}$; *Rosa26R*) embryos. White arowheads indicate βGal-positive, CD31-negative cord-like cell clusters, which were interspersed within capillaries. Scale bars, 50 μm.

clathrin-binding site in the N-terminal stretch, and relative resistance to PI3K inhibitors[16,18]. C2α is expressed in a limited number of cell types, including the epithelium, vascular endothelium and smooth muscle[19,20]. C2α localizes to clathrin-coated endocytic vesicles, other endosomes and the *trans*-Golgi network (TGN) and has been suggested to regulate intracellular vesicular trafficking[16,18,21,22]. Previous *in vitro* studies[21,23,24] showed that various extracellular stimuli, including cytokines, insulin and integrin ligation, modestly stimulate C2α activity. However, the *in vivo* function of C2α is largely unknown, although a recent study[25] showed that a hypomorphic C2α mutant allele resulted in impairment of renal glomerular formation.

Using a gene-targeting strategy, we explored the *in vivo* role of C2α. We found that C2α has a crucial role in developmental and pathological angiogenesis in an endothelial-cell–autonomous manner. Notably, the mechanisms underlying the proangiogenic effects of C2α differ from those of class I PI3Ks: C2α regulates primarily vesicular trafficking, which is essential for normal delivery of membrane proteins, including VE-cadherin, as well as for specific aspects of cellular signaling. C2α thus has a pivotal role in endothelial cell proliferation, survival, migration, morphogenesis and, thereby, angiogenesis. A second crucial role of C2α in the vasculature is maintenance of endothelial barrier function and vascular integrity.

RESULTS

Endothelial C2α is crucial for physiological angiogenesis

Homozygous global C2α-deleted mutant (*Pik3c2a*$^{-/-}$) mouse embryos had retarded growth from embryonic day (E) 8.5 and died between E10.5–E11.5 as a result of defects in vascular formation (**Fig. 1**, **Supplementary Table 1** and **Supplementary Figs. 1–3**), suggesting an essential nonredundant role of class II PI3Ks in mouse development. Whole-mount CD31 staining of the embryos revealed severe defects in vascular development throughout the embryo (**Fig. 1a**). In contrast to wild-type (*Pik3c2a*$^{+/+}$) embryos, the major vessels, including the dorsal aorta, intersomitic vessels and branchial arches, were severely disorganized or absent in *Pik3c2a*$^{-/-}$ embryos (**Fig. 1a**). We were barely able to detect α-smooth muscle actin (α-SMA)-positive

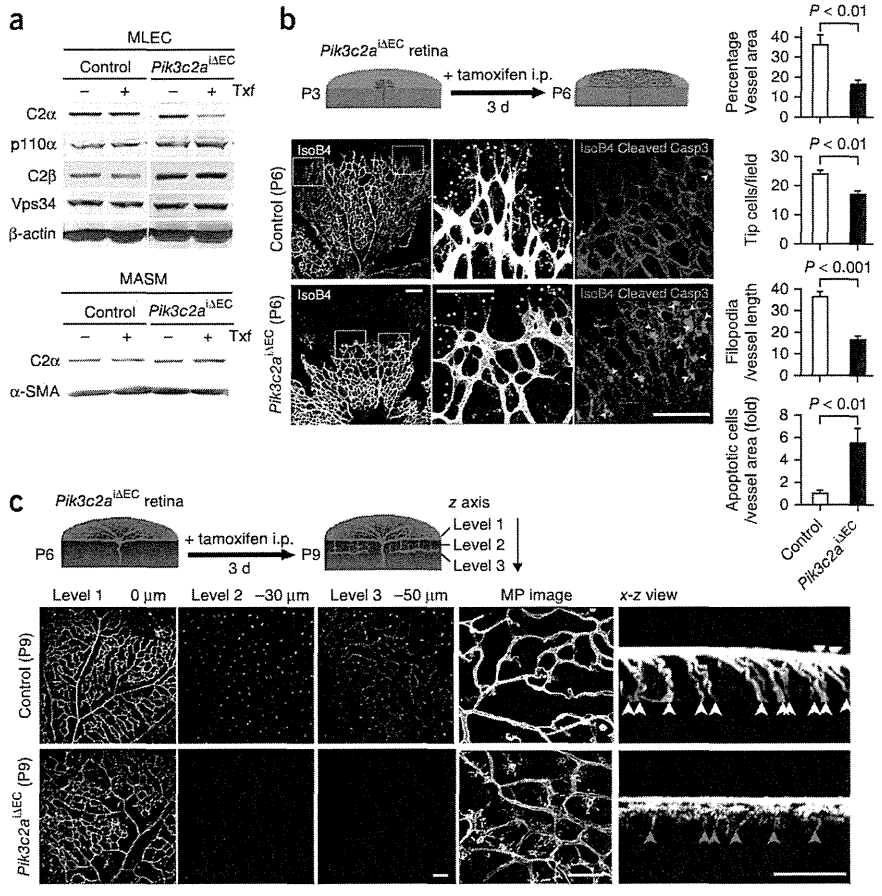

Figure 2 C2α is required for postnatal retinal angiogenesis. (**a**) Western blot analysis of C2α, p110α, C2β and Vps34 proteins in mouse lung endothelial cells (MLEC) and aortic smooth muscle cells (MASM) from 4-week-old control (*Pik3c2a*$^{flox/flox}$) and *Pik3c2a*$^{i\Delta EC}$ mice with or without administration of tamoxifen (Txf). β-actin and α-SMA were used as loading controls. (**b**) Top, schematic of the experimental strategy to assess early formation of the retinal vasculature (P3–P6) in *Pik3c2a*$^{i\Delta EC}$ mice. Bottom, flat-mount isolectin-B4 (IsoB4) staining of retinas from control (*Pik3c2a*$^{flox/flox}$) and tamoxifen (intraperitoneally (i.p.) administered at P3)-inducible endothelial-cell–specific C2α deletion mutant (*Pik3c2a*$^{i\Delta EC}$) mice at P6. Yellow dots and arrowheads indicate filopodia and apoptotic cells, respectively. Scale bars, 100 μm. Right, quantification of vessel area per microscopic field (%) and numbers of tip cells and filopodia per microscopic field. $n = 6–11$ mice per group. Casp3, caspase-3. Data shown are means ± s.e.m., and statistical significance was analyzed by Mann-Whitney *U* test. (**c**) Top, schematic of the experimental strategy to assess late development of the retinal vasculature (P6–P9) in *Pik3c2a*$^{i\Delta EC}$ mice. Bottom, flat-mount IsoB4 staining of retinas from control and *Pik3c2a*$^{i\Delta EC}$ mice at P9. At left, images of the sections at the indicated levels are shown. At right, maximum intensity projection (MIP) stacked confocal images and an *x-z* view of the retinal vasculature showing perpendicular sprouting (white and red arrowheads) at P9 in both groups are shown. Scale bars, 50 μm.

mural cells in the *Pik3c2a*$^{-/-}$ dorsal aorta, but could readily detect such cells in the hearts of *Pik3c2a*$^{-/-}$ and wild-type embryos (**Fig. 1b**). In support of the above data, at midgestation, C2α was highly expressed in vascular endothelial cells, as well as in other cell types, including SMC, cardiomyocytes and gastrointestinal epithelium of wild-type embryos (**Supplementary Fig. 4**).

To determine in which cell type(s) C2α is required, we generated three cardiovascular-specific C2α deletion strains (**Supplementary Fig. 5**). Both SMC-specific (*Pik3c2a*$^{flox/flox}$; *SM22a*-Cre, called here *Pik3c2a*$^{\Delta SMC}$) and cardiomyocyte-specific (*Pik3c2a*$^{flox/flox}$; *Nkx2-5*–Cre (ref. 26), called here *Pik3c2a*$^{\Delta CM}$) C2α-deletion mutants developed normally and the mutant animals were born at the expected Mendelian ratio (**Supplementary Tables 2** and **3**). However, the endothelial-cell–specific C2α-deletion mutant (*Pik3c2a*$^{flox/flox}$; *Tie2*-Cre (ref. 27), called here *Pik3c2a*$^{\Delta EC}$) has an embryonic-lethal phenotype (**Supplementary Tables 3–7**) involving abnormalities in multiple organs, including severely impaired vascular formation, indicating that endothelial C2α is essential for normal vascular formation and development. The most severely affected *Pik3c2a*$^{\Delta EC}$ mutants died at E12.5 and phenocopied a global *Pik3c2a*-null embryo. *Pik3c2a*$^{\Delta EC}$ embryos also had marked dilation of subcutaneous microvessels and hemorrhage (**Fig. 1c**). Double immunofluorescent staining of *Pik3c2a*$^{\Delta EC}$ embryo tissue using CD31- and α-SMA–specific antibodies showed reductions in vascular branching and in the area covered by endothelial cells (reduced by 31% and 36%, respectively, compared with control embryos; $P < 0.05$; **Fig. 1c,d**) and discontinuous and incomplete coverage of microvessels with SMC (**Fig. 1c** and **Supplementary Fig. 6a,b**). Immunostaining using VE-cadherin–specific and neuron-glial antigen 2 (NG2)-specific antibodies revealed that capillaries had discontinuous adherens-junction formation and poor coverage with NG2-positive pericytes, which were frequently rounded and had cellular processes that were detached from the capillary wall (**Fig. 1c** and **Supplementary Fig. 6c**). In *Pik3c2a*$^{\Delta EC}$; *Rosa26R* embryos, β-galactosidase–positive, CD31-negative cord-like cell clusters were interspersed within the capillaries (**Fig. 1e**), suggesting impaired endothelial-cell differentiation in the vasculature of *Pik3c2a*$^{\Delta EC}$ embryos. Taken together, these results imply that loss of C2α expression in endothelial cells is responsible for the phenotype of *Pik3c2a*$^{-/-}$ mice.

Because *Pik3c2a*$^{\Delta EC}$ mice are embryonic lethal, we created tamoxifen-inducible, conditional endothelial-cell–specific C2α-deletion mice (*Pik3c2a*$^{i\Delta EC}$) that expressed tamoxifen-activated Cre recombinase under the control of the VE-cadherin promoter[28] (*Pik3c2a*$^{flox/flox}$; *Cdh5*(PAC)-CreER^{T2}; **Supplementary Fig. 5e**). We studied the role of C2α in postnatal physiological angiogenesis in these mice using a retinal angiogenesis model. Administration of tamoxifen to these mice at postnatal day (P) 3 resulted in a marked reduction in C2α protein expression at P6 in endothelial cells isolated from the lungs but not in aortic SMC (**Fig. 2a**). At P6, endothelial-cell–specific C2α inactivation induced by tamoxifen administration markedly inhibited retinal angiogenesis: vessel area, the number of tip cells and the number of filopodia at the vascularizing front were reduced by 46%, 32% and 48%, respectively, in the superficial layer of retinas from *Pik3c2a*$^{i\Delta EC}$ mice compared with those from tamoxifen-administered *Pik3c2a*$^{flox/flox}$ control mice (**Fig. 2b** and **Supplementary Fig. 7**). Perpendicular vascular sprouting and horizontal vascular network formation in the deeper retina were also severely impaired in *Pik3c2a*$^{i\Delta EC}$ retinas (**Fig. 2c**). In addition, retinas of *Pik3c2a*$^{\Delta EC}$

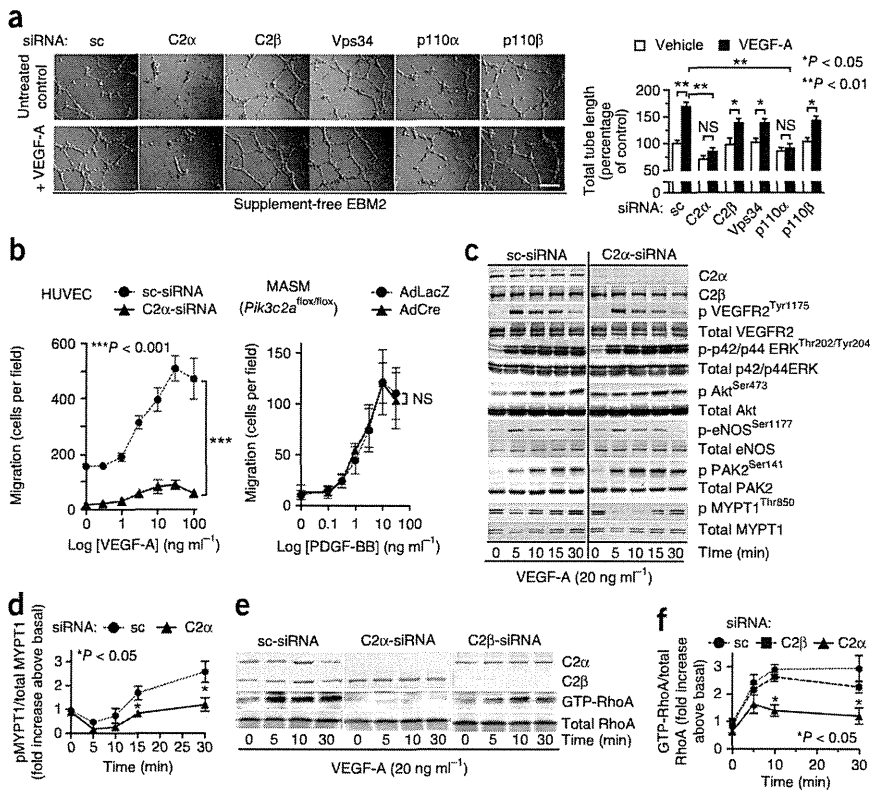

Figure 3 Tube formation, cell migration and RhoA activation are impaired in C2α-depleted HUVEC. (**a**) Effects of siRNA-mediated PI3K knockdown on VEGF-A (20 ng ml^{-1})-induced tube formation in serum-free and growth factor supplement–free medium. Scale bar, 200 μm. Quantification of total tube length (right). NS, not significant; sc, scrambled siRNA control. (**b**) Effects of C2α knockdown or deletion on VEGF-A–directed HUVEC migration and PDGF-BB–directed MASM migration. AdLacZ, adenovirus expressing β-galactosidase; AdCre, adenovirus expressing Cre. Data are means ± s.e.m. (**c**) Western blot analysis of the indicated proteins after treatment of control or C2α-depleted HUVEC following VEGF-A (20 ng ml^{-1}) treatment at the indicated time points. (**d**) Quantification of VEGF-A–induced phosphorylation of MYPT1. (**e**) Western blot analysis of the indicated proteins after treatment of control or C2α- or C2β-depleted HUVEC following VEGF-A (20 ng ml^{-1}) treatment at the indicated time points. (**f**) Quantification of the results in **e**. Data in **d** and **f** are shown as relative values of the normalized band intensities. For **a**, **b**, **d** and **f**, data shown are means ± s.e.m. of three independent experiments. Statistical significance was analyzed by two-way analysis of variance (ANOVA).

mice showed a marked (5.5-fold) increase in apoptosis compared to those of control littermates ($P < 0.01$; **Fig. 2b**). Mice with hemizygous *Pik3c2a* endothelial-cell–specific deletion (*Pik3c2a*$^{flox/+}$; *Tie2*-Cre mice) also showed decreased retinal angiogenesis with reduced numbers of tip cells and filopodia at the vascularizing front as well as reduced endothelial cell proliferation (**Supplementary Fig. 8**).

C2α is involved in endothelial cell function through RhoA

In human umbilical vein endothelial cells (HUVEC) cultured in serum and growth factor supplement–free medium, knockdown of either p110α or C2α by specific siRNAs, but not knockdown of other PI3Ks by C2β-, Vps34- or p110β-specific siRNAs, inhibited VEGF-A–induced capillary-like tube formation (**Fig. 3a** and **Supplementary Fig. 9a,b**). In HUVEC cultured in complete growth medium with serum and growth-factor supplements (endothelial basal medium 2 (EBM2)), knockdown of C2α inhibited tube formation, whereas knockdown of p110α or other PI3Ks did not have this effect; knockdown of p110α and p110β together inhibited tube formation of cells cultured in EBM2 (**Supplementary Fig. 9c**).

C2α knockdown also markedly inhibited transwell migration of HUVEC toward VEGF-A ($P < 0.001$; **Fig. 3b**) but not migration of SMC toward platelet-derived growth factor BB (PDGF-BB), augmented HUVEC apoptosis (**Supplementary Fig. 9d,e**) and modestly inhibited HUVEC serum-induced proliferation (**Supplementary Fig. 9f**). In contrast, Cre-mediated deletion of C2α had no effect on SMC proliferation (**Supplementary Fig. 9g**). These results indicate specific, essential roles for C2α in endothelial cell activities.

C2α silencing did not alter VEGF-A–induced phosphorylation of VEGF receptor 2 (VEGFR2), p42/p44 extracellular signal-regulated kinase (ERK), Akt, endothelial nitric oxide synthase (eNOS) or p21-activated kinase-2 (PAK2) (**Fig. 3c**), which is in contrast to the effects of p110α knockdown[10–13]. However, C2α knockdown markedly inhibited VEGF-A–induced phosphorylation of myosin phosphatase target subunit 1 (MYPT1), a substrate of Rho kinase (**Fig. 3c,d**), and activation of the small GTPase RhoA (**Fig. 3e,f**). Consistent with these results, immunostaining using an antibody that specifically recognizes the GTP-bound active form of RhoA (**Supplementary Fig. 10a**) showed that knockdown of either C2α or p110α suppressed VEGF-A–induced RhoA activation (**Supplementary Fig. 10b**). Knockdown of C2α but not p110α or Vps34 also inhibited serum and growth factor-induced activation of RhoA (**Supplementary Fig. 10c**). In addition, C2α knockdown reduced activation of two other small GTPases: Rac1 activation induced by VEGF-A and Rap1 activation induced by fibroblast growth factor 2 (FGF2) (**Supplementary Fig. 11**). Both Rac1 and Rap1 as well as RhoA help stabilize VE-cadherin at contacts between endothelial cells[5,29].

RhoA knockdown, as well as VE-cadherin knockdown, abolished VEGF-A–induced tube formation ($P < 0.01$; **Supplementary Fig. 12a,b**). In a mixed culture of HUVEC, in which cells expressing the dominant-negative RhoA mutant RhoA^{Asn19} were mixed with LacZ-transfected control cells, RhoA^{Asn19}-expressing HUVEC were rounded and did not form cell-cell contacts through cell protrusions as did control HUVEC (**Supplementary Fig. 12c,d**). Together, these observations suggest that C2α has an essential role in endothelial morphogenesis through mechanisms involving RhoA.

C2α is required for endosomal trafficking of VE-cadherin

To study effects of C2α on endosomal trafficking, we first transfected HUVEC with the PtdIns(3)P-specific probe monomeric red fluorescent protein (mRFP)-tagged 2 × FYVE domain[30,31]. In control HUVEC treated with scrambled (sc) siRNA, the mRFP-2 × FYVE signal was localized mainly to endosomes (**Fig. 4a**). Depletion of C2α, but not of p110α or Vps34, markedly reduced the number of mRFP-2 × FYVE$^+$ vesicles ($P < 0.01$). The total cellular content of PtdIns(3)P, but not of PtdIns(3,4)P_2, PtdIns(3,5)P_2 or PtdIns(3,4,5)P_3,

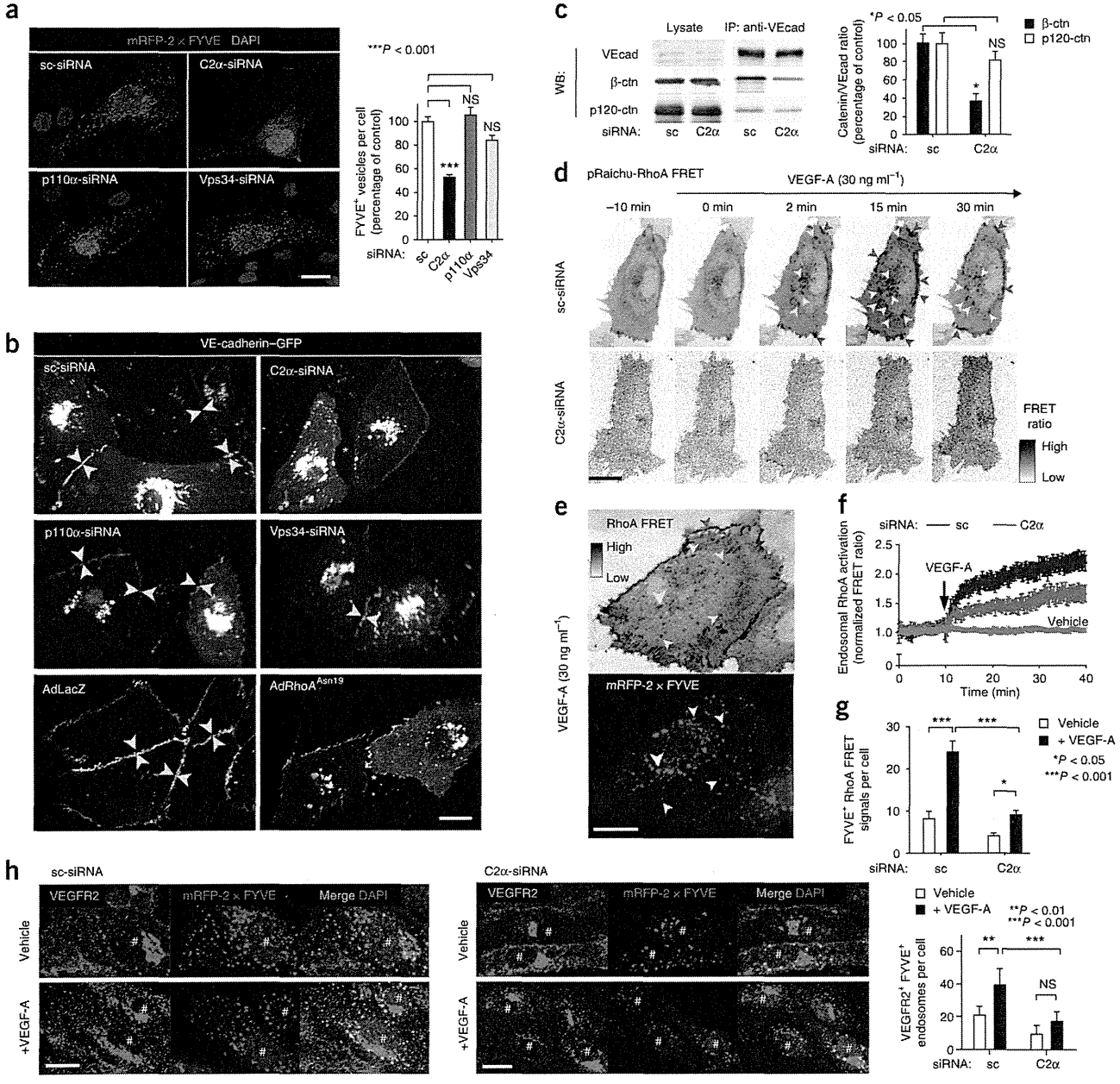

Figure 4 Endosomal transport, VE-cadherin assembly at cell junctions and the activation of endosomal RhoA are impaired in C2α-depleted endothelial cells. (**a**) Left, fluorescent imaging of sc-siRNA–treated control HUVEC and C2α-, p110α- or Vps34-depleted HUVEC transfected with the mRFP-2 × FYVE domain. Scale bar, 20 μm. Right, quantification of the number of mRFP-2 × FYVE$^+$ (FYVE$^+$) vesicles per cell. $n = 11–14$ cells per group. NS, not significant. (**b**) Fluorescent imaging of VE-cadherin–GFP trafficking in sc-siRNA–treated control HUVEC, C2α-, p110α- or Vps34-depleted HUVEC and AdLacZ- or AdRhoA^{Asn19}-transfected HUVEC. Yellow arrowheads indicate VE-cadherin$^+$ cell-cell contacts. Asterisks indicate gaps between HUVEC. Scale bar, 20 μm. See also **Supplementary Videos 4** and **5**. (**c**) Immunoprecipitation (IP) and western blot (WB) analyses to assess association of β-catenin (β-ctn) and p120-catenin (p120-ctn) with VE-cadherin (VEcad). VE-cadherin was immunoprecipitated from HUVEC treated with the indicated siRNAs, followed by western blotting for the indicated proteins. Western blots of the cell lysate without immunoprecipitiation are shown as a control. Quantification of the results is shown at right. Data from three independent experiments are shown. (**d–g**) HUVEC transfected with the FRET probe expression vector pRaichu-RhoA were used to assess RhoA activation. (**d**) At the indicated time points after treatment with VEGF-A, RhoA activation was visualized on endosomes (yellow arrowheads) and on plasma membrane at cell-cell contacts (red arrowheads) in control (sc-siRNA) and C2α-depleted HUVEC. (**e**) VEGF-A–induced RhoA activation in HUVEC cotransfected with pRaichu-RhoA and mRFP-2 × FYVE. Colocalization was observed between FRET signals (yellow arrowheads, top) and mRFP-2 × FYVE$^+$ endosomes (white arrowheads, bottom). Red arrowheads (top) indicate RhoA activation at cell-cell contacts. Scale bar, 20 μm. (**f**) Quantification of endosomal RhoA activation in control and C2α-depleted HUVEC at the indicated time ponts after VEGF or vehicle (M199 medium) addition. $n \geq 8$ cells per group. (**g**) Quantification of mRFP-2 × FYVE$^+$ FRET signals in HUVEC 15 min after VEGF-A or vehicle addition. $n = 9–22$ cells per group. (**h**) Immunofluorescence staining of VEGFR2 (green) and mRFP-2 × FYVE staining in cells cotransfected with the mRFP-2 × FYVE construct and either sc-siRNA or C2α-targeting siRNA. The cells were treated with VEGF-A or vehicle as indicated. Quantification of the number of VEGFR2$^+$ FYVE$^+$ endosomes per cell is shown at right. #, mRFP-2 × FYVE–transfected cells. $n = 8–20$ cells per group. Scale bars, 20 μm. In **a**, **c**, **g** and **h**, data shown are means ± s.e.m. Statistical significance was analyzed by one-way ANOVA for **a** and two-way ANOVA for **c**, **g** and **h**.

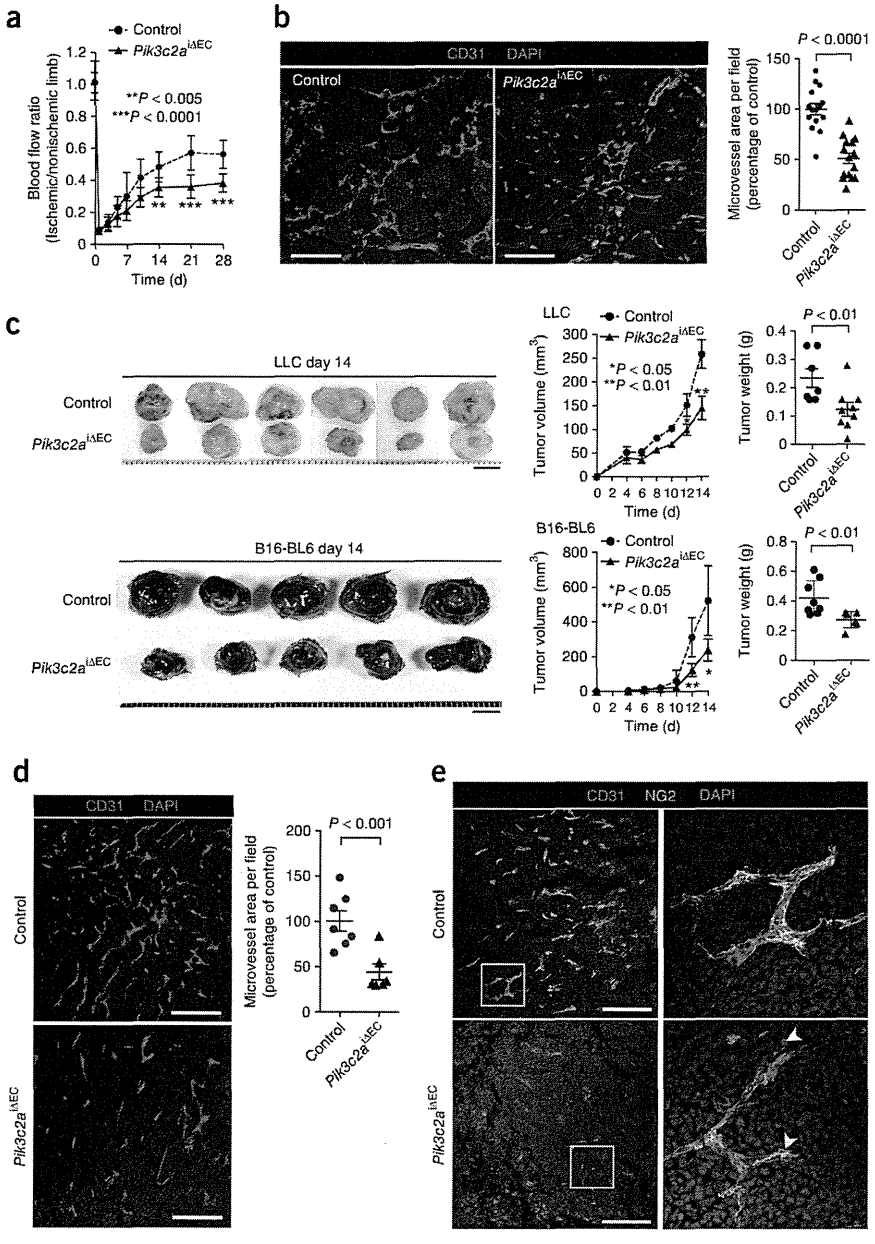

Figure 5 Targeted deletion of endothelial C2α reduces postischemic and tumor angiogenesis. (**a**,**b**) Postischemic hindlimb angiogenesis. (**a**) The ratio of ischemic to nonischemic limb laser Doppler blood flow in male 8-week-old control (*Pik3c2a*$^{flox/flox}$) and homozygous endothelial-cell–specific C2α deletion mutant (*Pik3c2a*$^{i\Delta EC}$) mice at the indicated time points following ischemic injury. $n = 13$ mice per group. Data shown are means ± s.e.m. Statistical significance was analyzed by two-way ANOVA. (**b**) CD31-specific immunofluorescence staining of sections of ischemic hindlimb muscle in control and *Pik3c2a*$^{i\Delta EC}$ mice. Nuclei (blue) were stained with DAPI. Scale bars, 100 μm. Quantification of CD31$^+$ microvessel density on day 28 after injury is shown at right. $n \geq 20$ fields from at least eight mice. Statistical significance was analyzed by Mann-Whitney *U* test. (**c**) Representative LLC (top) and B16-BL6 tumors (bottom) in male 10-week-old control and *Pik3c2a*$^{i\Delta EC}$ mice. Scale bars, 5 mm. Quantification of tumor volume and weight (day 14) is shown at right. $n \geq 7$ mice per group. Data shown are means ± s.e.m. (**d**) CD31-specific immunofluorescence staining of LLC tumor sections in control and *Pik3c2a*$^{i\Delta EC}$ mice. Scale bars, 200 μm. Quantification of CD31$^+$ microvessel density is shown at right. $n = 7$ mice per group. Statistical significance was analyzed by two-way ANOVA for tumor volumes and by Mann-Whitney *U* test for tumor weights. (**e**) CD31- and NG2-specific double immunofluorescence staining of LLC tumor sections in control and *Pik3c2a*$^{i\Delta EC}$ mice. Yellow and white arrowheads indicate loose attachment and detachment of pericytes, respectively, in *Pik3c2a*$^{i\Delta EC}$ mice. Scale bars, 200 μm. Nuclei (blue) were stained with DAPI.

was reduced in C2α-depleted cells compared to control cells (**Supplementary Fig. 13**). Thus, C2α is needed for normal PtdIns(3)P accumulation in the endosomal compartment. Consistent with this idea, we detected C2α in a granular pattern in HUVEC, with enrichment in the perinuclear region, and found that C2α partially colocalized with markers of clathrin-coated vesicles, the TGN and early endosomes (**Supplementary Fig. 14a–c**)[16,18,22]. The intracellular localization of GFP-C2α also substantially overlapped with that of mRFP-2 × FYVE (**Supplementary Fig. 15a** and **Supplementary Video 1**). The motility, fusion and fission of GFP-tagged 2 × FYVE$^+$ vesicles were markedly attenuated in C2α-depleted cells (**Supplementary Videos 2** and **3**), suggesting that C2α is involved in endosomal trafficking. Knockdown of C2α, but not of p110α or Vps34, caused enlargement of the Golgi and TGN area (**Supplementary Fig. 14d**). We also found swelling of the Golgi and TGN compartment in endothelial cells of dorsal aortas from *Pik3c2a*$^{-/-}$ mice, as assessed by electron microscopy (**Supplementary Fig. 14e**).

In C2α-depleted but not p110α- or Vps34-depleted HUVEC, the trafficking of VE-cadherin between the TGN and intercellular junctions at the plasma membrane was disrupted (**Fig. 4b** and **Supplementary Videos 4** and **5**). C2α was partially colocalized with VE-cadherin in the Golgi and TGN area and in endosomes but this colocalization was not evident at intercellular junctions (**Supplementary Fig. 15b**). A portion of the mRFP-2 × FYVE$^+$ vesicles were positive for VE-cadherin–GFP, suggesting transport of VE-cadherin by PtdIns(3)P$^+$ vesicles (**Supplementary Fig. 15c**). In agreement with these findings, the accumulation of VE-cadherin at cell-cell contacts in C2α-depleted but not p110α- or Vps34-depleted HUVEC was reduced and the staining for VE-cadherin was discontinuous (**Supplementary Fig. 16b**). C2α-depleted cells also showed a reduced association of VE-cadherin with β-catenin as well as instability of VE-cadherin protein (**Fig. 4c** and **Supplementary Fig. 16a**). Expression of RhoA^{Asn19} in HUVEC impaired VE-cadherin trafficking between the TGN and the plasma membrane, resulting in disturbed VE-cadherin clustering at cell-cell contacts (**Fig. 4b**, **Supplementary Video 6** and **Supplementary Fig. 16c**). In mixed cultures of normal and RhoA-depleted HUVEC, VE-cadherin clustering was impaired at the boundaries between RhoA-depleted cells (**Supplementary Fig. 16d**). In C2α-depleted HUVEC, expression

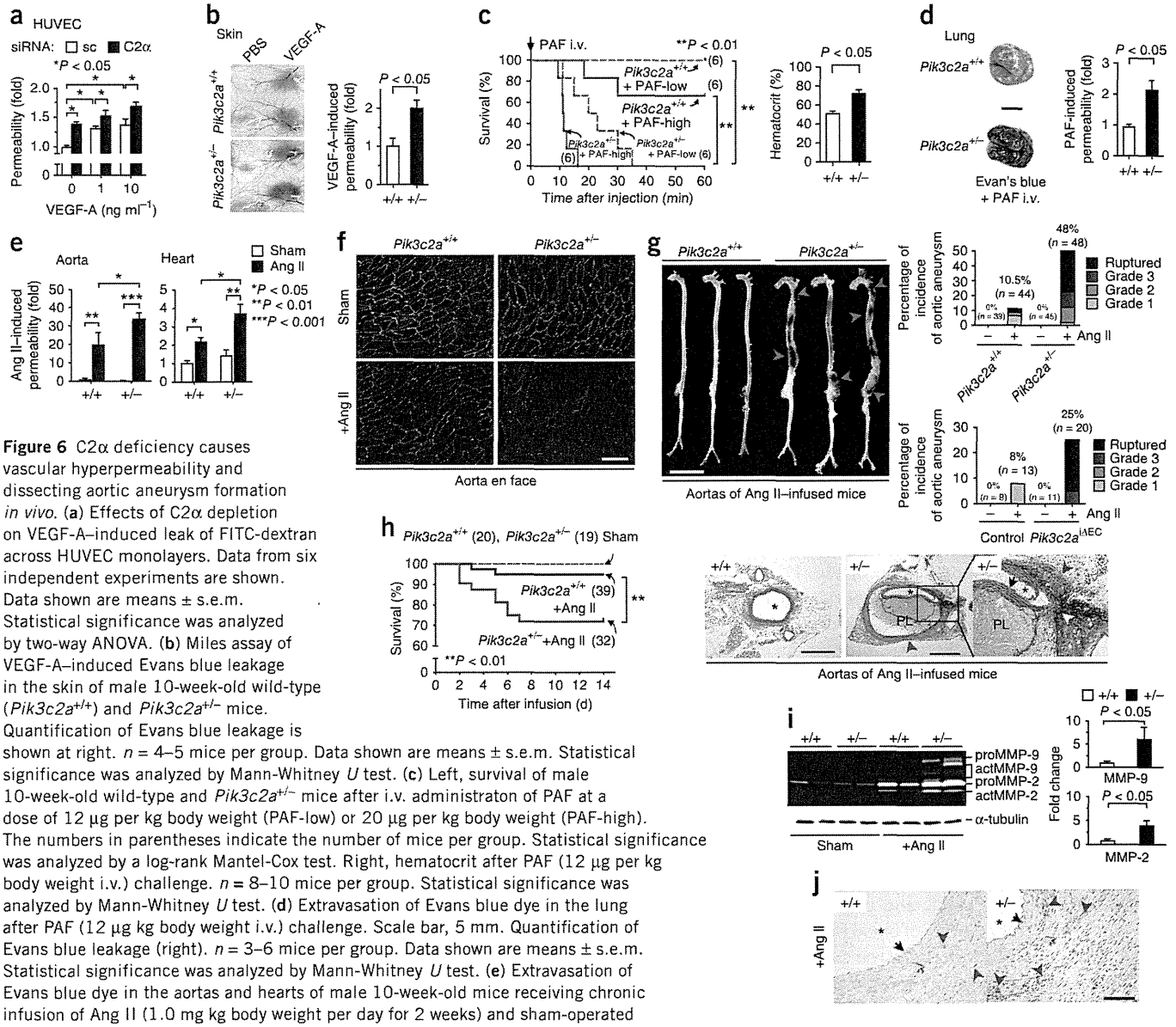

Figure 6 C2α deficiency causes vascular hyperpermeability and dissecting aortic aneurysm formation *in vivo*. (**a**) Effects of C2α depletion on VEGF-A–induced leak of FITC-dextran across HUVEC monolayers. Data from six independent experiments are shown. Data shown are means ± s.e.m. Statistical significance was analyzed by two-way ANOVA. (**b**) Miles assay of VEGF-A–induced Evans blue leakage in the skin of male 10-week-old wild-type (*Pik3c2a*$^{+/+}$) and *Pik3c2a*$^{+/-}$ mice. Quantification of Evans blue leakage is shown at right. $n = 4$–5 mice per group. Data shown are means ± s.e.m. Statistical significance was analyzed by Mann-Whitney *U* test. (**c**) Left, survival of male 10-week-old wild-type and *Pik3c2a*$^{+/-}$ mice after i.v. administraton of PAF at a dose of 12 μg per kg body weight (PAF-low) or 20 μg per kg body weight (PAF-high). The numbers in parentheses indicate the number of mice per group. Statistical significance was analyzed by a log-rank Mantel-Cox test. Right, hematocrit after PAF (12 μg per kg body weight i.v.) challenge. $n = 8$–10 mice per group. Statistical significance was analyzed by Mann-Whitney *U* test. (**d**) Extravasation of Evans blue dye in the lung after PAF (12 μg kg body weight i.v.) challenge. Scale bar, 5 mm. Quantification of Evans blue leakage (right). $n = 3$–6 mice per group. Data shown are means ± s.e.m. Statistical significance was analyzed by Mann-Whitney *U* test. (**e**) Extravasation of Evans blue dye in the aortas and hearts of male 10-week-old mice receiving chronic infusion of Ang II (1.0 mg kg body weight per day for 2 weeks) and sham-operated control mice. $n = 3$–5 mice per group. Data shown are means ± s.e.m. Statistical significance was analyzed by two-way ANOVA. (**f**) En face confocal microscopic views of VE-cadherin–specific immunofluorescent staining of aortas from male 10-week-old mice treated with Ang II. Scale bar, 50 μm. (**g**) Aneurysm formation in *Pik3c2a*$^{+/+}$ and *Pik3c2a*$^{+/-}$ mice treated with Ang II. Top left, gross view of aortic aneurysms (red arrowheads, top left). Scale bar, 1 mm. Top right, incidence and severity of aortic aneurysms in AngII-treated and nontreated, sham-operated *Pik3c2a*$^{+/-}$ and *Pik3c2a*$^{i\Delta EC}$ mice. See the Online Methods for how aneurysm severity was graded. Bottom, azan-stained sections of dissecting aortic aneurysm in AngII-treated *Pik3c2a*$^{+/-}$ mice. Scale bars, 500 μm. PL, pseudolumen; red arrowheads, adventitia; black arrow, internal elastic lamina; yellow arrow, external elastic lamina; asterisks, true lumen of the aorta. (**h**) Survival of Ang II-treated and nontreated, sham-operated male 8- to 10-week-old *Pik3c2a*$^{+/+}$ and *Pik3c2a*$^{+/-}$ mice. The numbers in parentheses indicate the number of mice in each group. Statistical significance was analyzed by a log-rank Mantel-Cox test. (**i**) Left, MMP-2 and MMP-9 activity as assessed by zymography in the aortas of Ang II-treated and nontreated, sham-operated 10-week-old male *Pik3c2a*$^{+/+}$ and *Pik3c2a*$^{+/-}$ mice. proMMP-2 and proMMP-9, MMP-2 and MMP-9 proenzymes; actMMP-2 and actMMP-9, active MMP-2 and MMP-9. Right, quantification of MMP-2 and MMP-9 activities. The sum of the proMMP-2 and actMMP-2 band densities and the sum of the proMMP-9 and actMMP-9 band densities were defined as MMP-2 and MMP-9 total activities, respectively. $n = 6$ mice per group. Data shown are means ± s.e.m. Statistical significance was analyzed by Mann-Whitney *U* test. (**j**) Mac-3–specific immunohistochemical staining of the aortic walls of male *Pik3c2a*$^{+/+}$ and *Pik3c2a*$^{+/-}$ 10-week-old mice treated with Ang II. Red arrowheads, infiltrating macrophages; black arrows, internal elastic lamina; yellow arrows, external elastic lamina. Scale bar, 200 μm.

of a GFP-tagged constitutively active RhoA mutant, Rho^{Val14}, but not of GFP-tagged wild-type RhoA, partially restored defective VE-cadherin clustering at cell-cell contacts (**Supplementary Fig. 16e**). In contrast, in sc-siRNA–treated control HUVEC, expression of GFP-tagged RhoA^{Asn19}, but not of GFP-tagged wild-type RhoA, attenuated VE-cadherin assembly at cell junctions. Thus, RhoA is required for VE-cadherin assembly at the cell junctions of endothelial cells.

As our results indicate that C2α is necessary for endosomal trafficking, and as endosomes are now recognized as being involved in the activation of signaling molecules, including Rho GTPases[32], we next explored where C2α-dependent RhoA activation occured in cells. We visualized RhoA activation by adopting a fluorescence resonance energy transfer (FRET) imaging technique. We transfected HUVEC with an expression vector for a chimeric RhoA-FRET probe protein,

Raichu-RhoA, which comprises N-terminal yellow fluorescent protein (YFP), the Rho-binding domain of protein kinase N, RhoA and C-terminal cyan fluorescent protein (CFP). GTP loading into the RhoA domain of Raichu-RhoA protein results in an intramolecular conformational change of Raichu-RhoA, which increases FRET efficiency. By fluorescent microscopic observation, we could localize RhoA activation sites within cells. In HUVEC, RhoA was activated in both the intracellular vesicular compartment and the plasma membrane, with intense signals at cell-cell contacts (**Fig. 4d** and **Supplementary Video 7**). A substantial portion of the intracellular FRET signal coincided with mRFP-2 × FYVE signals (**Fig. 4e**). C2α knockdown reduced the RhoA FRET signal in both the endosomes and the plasma membrane (**Fig. 4d–g** and **Supplementary Video 8**), indicating that C2α is necessary for RhoA activation in PtdIns(3)P-enriched endosomes and in the plasma membrane. We further studied the role of C2α in VEGF receptor internalization, which might occur upstream of RhoA activation[33]. VEGF-A stimulated the internalization of VEGFR2 into the 2 × FYVE$^+$ vesicular compartment, which was dampened by C2α depletion (**Fig. 4h**). VEGF-A induced phosphorylation of VEGFR2 at the plasma membrane 2 min after stimulation; at 30 min after stimulation, most phosphorylated VEGFR2 was redistributed in the intracellular compartment, primarily in early endosome antigen 1 (EEA1)$^+$ endosomes (**Supplementary Fig. 17**). C2α depletion did not inhibit the initial VEGFR2 phosphorylation in the plasma membrane but did inhibit the internalization of phosphorylated VEGFR2 (**Supplementary Fig. 17**). Furthermore, treatment with dynasore, an inhibitor of dynamin-dependent endocytosis[34], inhibited growth-factor–induced RhoA activation, VE-cadherin assembly at cell junctions and tube formation (**Supplementary Fig. 18a–d**). Thus, C2α is essential for the internalization of activated VEGF receptors, activation of RhoA and other signaling molecules on endosomes, RhoA-dependent trafficking and assembly of VE-cadherin at cell junctions.

Endothelial C2α is essential for pathological angiogenesis

We next studied the role of endothelial C2α in pathological angiogenesis using postischemic and tumor angiogenesis models. In *Pik3c2a*$^{i\Delta EC}$ mice, the recovery of blood flow in the ischemic hindlimb after surgical femoral arteriectomy was suppressed during postoperative days 14–28 compared to the recovery in control *Pik3c2a*$^{flox/flox}$ mice ($P < 0.0001$ on day 28; **Fig. 5a**). Immunofluorescence staining using a CD31-specific antibody showed an approximately 50% decrease in microvessel density in the ischemic muscle of *Pik3c2a*$^{i\Delta EC}$ mice compared to control mice on postoperative day 28 ($P < 0.0001$; **Fig. 5b**).

After implantation of Lewis lung carcinoma (LLC) or B16-BL6 melanoma tumors, *Pik3c2a*$^{i\Delta EC}$ mice had diminished tumor volumes and weights compared with those of control *Pik3c2a*$^{flox/flox}$ mice ($P < 0.05$; **Fig. 5c**). The microvessel density in LLC tumors was reduced in *Pik3c2a*$^{i\Delta EC}$ mice compared to that in control mice ($P < 0.05$; **Fig. 5d**). Moreover, double immunostaining with CD31- and NG2-specific antibodies revealed that tumor microvessels in *Pik3c2a*$^{i\Delta EC}$ mice had poor coverage with NG2$^+$ pericytes, which were frequently rounded or detached from the microvessels (**Fig. 5e**).

C2α is required for vascular barrier function and integrity

The permeability of a monolayer of C2α-depleted HUVEC was increased under both resting and VEGF-A–stimulated conditions compared with that of control cells under the same conditions ($P < 0.05$; **Fig. 6a**). After VEGF-A injection, the increase in the leakage of intravenously administered Evans blue dye into the skin was greater in *Pik3c2a*$^{+/-}$ mice than in wild-type mice ($P < 0.05$; **Fig. 6b**). We next studied vascular responses to other hyperpermeability- and inflammation-eliciting insults in global *Pik3c2a*$^{+/-}$ and wild-type mice. Intravenous (i.v.) injection of a low dose of platelet-activating factor (PAF), a mediator of anaphylactic shock[35], did not affect survival in wild-type mice, whereas it induced death in all *Pik3c2a*$^{+/-}$ littermates within 40 min, with accompanying increases in hematocrit levels and Evans blue leakage in the lung (**Fig. 6c,d**). A higher dose of PAF, which induced death in a portion (about 30%) of wild-type mice, caused more rapid death of all *Pik3c2a*$^{+/-}$ mice (**Fig. 6c**). PAF-induced increases in plasma histamine and interleukin-4 (IL-4) concentrations, both of which are anaphylactic mediators, were similar in wild-type and *Pik3c2a*$^{+/-}$ mice (**Supplementary Fig. 19**), suggesting that C2α deficiency impairs endothelial function, resulting in vascular barrier disruption.

Chronic Ang II infusion induced more robust hyperpermeability in the aorta and coronary vessels in *Pik3c2a*$^{+/-}$ mice than in wild-type littermates (**Fig. 6e**). En face immunostaining of the aorta using a VE-cadherin–specific antibody showed disorganization of adherens junctions in AngII-treated *Pik3c2a*$^{+/-}$ mice (**Fig. 6f**). Concomitantly, we found a higher incidence of aortic aneurysms with dissection, resultant rupture and death in *Pik3c2a*$^{+/-}$ mice compared with wild-type littermates (aneurysm occurred in 23/48 *Pik3c2a*$^{+/-}$ mice and 5/44 wild-type mice) ($P < 0.01$; **Fig. 6g,h**). Conditional endothelial-cell–specific deletion of C2α also resulted in a higher occurrence of dissecting aneurysms compared to control mice (aneurysm occurred in 5/20 *Pik3c2a*$^{i\Delta EC}$ mice and 1/13 control mice) ($P < 0.01$; **Fig. 6g**). There was no difference in blood pressure between AngII-treated *Pik3c2a*-deleted and control mice (data not shown). Thus, the aortic walls of C2α-deficient mice seem to be fragile compared with those of wild-type mice. Ang II infusion stimulated matrix metalloproteinase 2 (MMP-2) and MMP-9 activities, which have been implicated in the formation of aneurysms in aortic tissue[6,7,36,37]; these increases were greater in *Pik3c2a*$^{+/-}$ mice than in wild-type mice ($P < 0.05$; **Fig. 6i**). Immunostaining using an antibody to Mac-3, a macrophage marker, revealed a greater number of infiltrating macrophages (the major source of MMPs), found primarily in the aortic adventitia, in *Pik3c2a*$^{+/-}$ mice compared with wild-type mice (**Fig. 6j**).

DISCUSSION

This study shows that in endothelial cells, PI3K-C2α, a class II PI3K, has indispensable roles in sprouting angiogenesis and subsequent mural-cell recruitment and in maintaining vascular barrier integrity in quiescent vessels. C2α deficiency results in impaired angiogenesis and pathological vascular hyperpermeability with vascular damage. At the cellular level, C2α is essential for endothelial cell migration, proliferation and survival and VE-cadherin assembly at intercellular junctions. The actions of C2α are mediated by its regulatory effects on intracellular vesicular transport; that is, on the delivery and recycling of membrane molecules and on cell signaling that likely occurs on endosomes (**Supplementary Fig. 20**). These actions of C2α underlie its roles in angiogenesis and barrier integrity. The actions of C2α and of class I PI3Ks in endothelial cells are distinct: in contrast to C2α, class I PI3Ks have a large effect on Akt stimulation and cell proliferation but are not involved in vesicular trafficking and do not affect VE-cadherin trafficking to the plasma membrane or VE-cadherin assembly at the cell-cell junction[10–13]. Therefore, these observations reveal new biological activities of C2α and underscore broader roles for PI3K family members in vascular physiology and pathophysiology.

In contrast to class I PI3Ks that generate PtdIns(3,4,5)P_3, the major product of class II and III PI3Ks is PtdIns(3)P, which accumulates mainly in endosomes[16–18,20–25]. Consistent with this, C2α in endothelial cells was localized in endosomes and the TGN, organelles that are responsible for the processing, sorting and packaging of proteins for transport to their final destinations. Another class II PI3K, PI3K-C2β, and the class III PI3K Vps34 are also localized primarily in the clathrin-coated or endocytic compartment[38,39]. Localized production of PtdIns(3)P in conjunction with the presence of Rab GTPases, such as Rab5, on the endocytic membrane cause the recruitment of proteins such as EEA1 and rabenosyn-5; this recruitment facilitates dynamic formation of endocytic membranous structures for uptake, packaging and sorting[31,32,39]. Our results show that C2α is the PI3K isoform in endothelial cells that is largely responsible for PtdIns(3)P accumulation on endosomes. C2α seems to have a functionally distinct role from that of C2β or Vps34, as depletion of C2α, but not Vps34 or C2β, severely impairs trafficking of 2 × FYVE$^+$ vesicles and transport and assembly of VE-cadherin, and C2α deficiency impairs receptor internalization and VE-cadherin trafficking. Thus, C2α in endothelial cells may be located in a different endocytic compartment compared to C2β and Vps34 cells, or C2α activity may be regulated differently compared to the activities of C2β and Vps34 (refs. 18,23,40). Therefore, C2α has specialized functions in vesicular trafficking in endothelial cells.

Our data also show that C2α is involved in cell signaling. Endocytosis has long been recognized as a mechanism for terminating signaling by internalizing and degrading cell-surface receptors[41]. Besides this classical role of endocytosis, recent studies[32,41–43] have shown that endosomes serve as platforms to assemble membrane receptors and their downstream signaling molecules and to generate spatially localized signals. In endothelial cells, activation of RhoA, Rac1 and Rap1, but not of Akt or ERK, is dependent on C2α to varying degrees, indicating that the generation of certain intracellular signals requires C2α. In particular, C2α is essential for the internalization of activated VEGFR2 and endosomal RhoA activation. Consistent with the role of endosomes in receptor signaling, blockade of endocytosis suppressed VEGF-A–induced RhoA activation. Localized activation of RhoA was recently shown to be necessary for the proper assembly of VE-cadherin at intercellular junctions and for barrier-protective activity[44,45], although there is also evidence for an opposite barrier-disruptive activity of RhoA[4,46,47]. Our data indicate that C2α-dependent RhoA activity on endosomes is crucial for the delivery and assembly of VE-cadherin at cell contacts and for cell-cell contact formation. The identity of the Rho-guanine nucleotide exchange factor (Rho-GEF) that is responsible for VEGF-induced endosomal RhoA activation in endothelial cells, as well as the molecular mechanisms involved in the recruitment and activation of this factor, remain to be determined. Rap1 and Rac1 have also been implicated in strengthening VE-cadherin–mediated intercellular junctions[4,46,48].

The effects of C2α on endosomal transport and signaling may have a pivotal role in endothelial cell migration, proliferation and survival and vascular morphogenesis. For example, Rho and Rac are activated at the rear and front ends, respectively, of migrating cells to drive machinery responsible for retracting the rear portion of the cell body and extending protrusions forward[49]. During cell migration, there is assembly and disassembly of focal adhesions, which depends on endocytic and recycling vesicular functions[49,50]. Rho GTPases are involved in the formation of focal adhesions, which generate cell-survival signals through mechanisms involving integrin ligation. Polarization of the endothelial cell monolayer in the vascular wall also depends on membrane trafficking[51]. Endosomes could be involved in these processes, both by serving as a platform for the activation of Rho GTPases and recruiting Rho GTPases to specific sites within cells[45]. Taken together, our observations strongly suggest that C2α has a role in angiogenesis and vascular integrity through its regulation of vesicular trafficking.

In adult mice, C2α expression is generally diminished compared with its expression in embryos, but it is still expressed at an easily detectable level in the vascular endothelium among other tissues[19]. Our data show that C2α is essential for maintaining barrier integrity in quiescent vessels, as evidenced by its protective role in diminishing VEGF-A–induced hyperpermeability. In anaphylaxis, a 50% reduction in C2α expression markedly increased mortality. In chronic vascular injury induced by Ang II infusion, disruption of the vascular wall probably caused by disassembly of VE-cadherin in the endothelium occurs, leading to fatal dissecting aneurysm formation. Collectively, our data are consistent with the notion that a normal level of C2α expression is essential for the maintenance of vascular integrity in quiescent vasculature, as well as for neovesssel formation. These observations point to the possibility that C2α may be a new therapeutic target for vascular diseases caused by barrier disruption.

METHODS

Methods and any associated references are available in the online version of the paper.

Note: Supplementary information is available in the online version of the paper.

ACKNOWLEDGMENTS

We thank K. Mitsumori for comments on the histological study. We thank N. Mochizuki and K. Ando for assistance with the FRET imaging analysis. We thank N. Furusawa, K. Sunagawa and E. Kaneko for assistance with live-cell imaging using a Yokogawa confocal microscope system. We also thank Y. Ohta and T. Murakawa for technical assistance and T. Hirose for administrative assistance. C2α complementary DNA was obtained from J. Domin (Imperial College London). GFP-2 × FYVE and mRFP-2 × FYVE expression vectors were obtained from H. Stenmark (Oslo University Hospital) and Y. Ohsumi (Tokyo Institute of Technology), respectively. VE-cadherin-GFP expression vectors were obtained from N. Mochizuki (National Cerebral and Cardiovascular Center). The pRaichu-RhoA probe was obtained from M. Matsuda (Kyoto University). GFP-RhoA^{Asn19} and GFP-RhoA^{Val14} expression vectors were obtained from F. Valderrama (King's College London). This work was supported in part by grants-in-aid from the Japanese Ministry of Education, Culture, Sports, Science and Technology, the Japan Society for the Promotion of Science (to K. Yoshioka, N. Takuwa, Y.O. and Y.T.), the Honjin Foundation, the Mitsubishi Pharma Research Foundation and the SENSIN Medical Research Foundation (to K. Yoshioka).

AUTHOR CONTRIBUTIONS

K. Yoshioka designed the experiments, performed characterization of the developmental and retinal angiogenesis of the conditional knockout mice and most of the *in vitro* studies and analyzed the data with assistance from N. Takuwa, Y.O., W.D., S.A., H.M., C.N., K.B., M.U., N. Takakura and O.M. K.A. and T.S. analyzed the cellular content of phosphoinositides. K. Yoshida performed *in vivo* angiogenenesis experiments with K. Yoshioka, performed tumor implantation and aneurysm experiments and interpreted the results. H.C. performed the anaphylaxis experiments. W.D. performed the *in vivo* permeability study. X.Q. and Y.O. performed and interpreted the results of the ischemic angiogenesis model. T.W. and S.I. performed and interpreted the results of electron microscopy. K.S., M.A., N. Takuwa, R.J.S., H.O. and R.H.A. generated mouse mutants. K. Yoshioka and Y.T. planned and supervised the experiments, arranged the figures and wrote the manuscript. M.A. and N. Takuwa participated in writing the manuscript (M.A. wrote part of the Online Methods, and N. Takuwa wrote the Abstract, Introduction and Results sections).

COMPETING FINANCIAL INTERESTS

The authors declare no competing financial interests.

Published online at http://www.nature.com/doifinder/10.1038/nm.2928.
Reprints and permissions information is available online at http://www.nature.com/reprints/index.html.

1. Adams, R.H. & Alitalo, K. Molecular regulation of angiogenesis and lymphangiogenesis. *Nat. Rev. Mol. Cell Biol.* **8**, 464–478 (2007).
2. Coultas, L. *et al.* Endothelial cells and VEGF in vascular development. *Nature* **438**, 937–945 (2005).
3. Andrae, J. *et al.* Role of platelet-derived growth factor in physiology and medicine. *Genes Dev.* **22**, 1276–1312 (2008).
4. Mehta, D. & Malik, A.B. Signaling mechanisms regulating endothelial permeability. *Physiol. Rev.* **86**, 279–367 (2006).
5. Dejana, E., Tournier-Lasserve, E. & Weinstein, B.M. The control of vascular integrity by endothelial cell junctions: molecular basis and pathological implications. *Dev. Cell* **16**, 209–221 (2009).
6. Yoshimura, K. *et al.* Regression of abdominal aortic aneurysm by inhibition of c-Jun N-terminal kinase. *Nat. Med.* **11**, 1330–1338 (2005).
7. Satoh, K. *et al.* Cyclophilin A enhances vascular oxidative stress and the development of angiotensin II–induced aortic aneurysms. *Nat. Med.* **15**, 649–656 (2009).
8. Ferrara, N. & Kerbel, R.S. Angiogenesis as a therapeutic target. *Nature* **438**, 967–974 (2005).
9. Carmeliet, P. Angiogenesis in life, disease and medicine. *Nature* **438**, 932–936 (2005).
10. Engelman, J.A. *et al.* The evolution of phosphatidylinositol 3-kinases as regulator of growth and metabolism. *Nat. Rev. Genet.* **7**, 606–619 (2006).
11. Takenawa, T. & Suetsugu, S. The WASP-WAVE protein network: connecting the membrane to the cytoskeleton. *Nat. Rev. Mol. Cell Biol.* **8**, 37–48 (2007).
12. Vanhaesebroeck, B. *et al.* The emerging mechanisms of isoform-specific PI3K signaling. *Nat. Rev. Mol. Cell Biol.* **11**, 329–341 (2010).
13. Graupera, M. *et al.* Angiogenesis selectively requires the p110α isoform of PI3K to control endothelial cell migration. *Nature* **453**, 662–666 (2008).
14. Yuan, T.L. & Cantley, L.C. PI3K pathway alterations in cancer: variations on a theme. *Oncogene* **27**, 5497–5510 (2008).
15. Funderburk, S.F. *et al.* The Beclin 1–Vps34 complex at the crossroads of autophagy and beyond. *Trends Cell Biol.* **20**, 355–362 (2010).
16. Falasca, M. *et al.* The role of phosphoinositide 3-kinase C2α in insulin signaling. *J. Biol. Chem.* **282**, 28226–28236 (2007).
17. Linassier, C. *et al.* Molecular cloning and biochemical characterization of a *Drosophila* phosphatidylinositol-specific phosphoinositide 3-kinase. *Biochem. J.* **321**, 849–856 (1997).
18. Domin, J. *et al.* The class II phosphoinositide 3-kinase PI3K-C2α is concentrated in the trans-Golgi network and present in clathrin-coated vesicles. *J. Biol. Chem.* **275**, 11943–11950 (2000).
19. El Sheikh, S.S. *et al.* Topographical expression of class IA and class II phosphoinositide 3-kinase enzymes in normal human tissues is consistent with a role in differentiation. *BMC Clin. Pathol.* **3**, 4 (2003).
20. Yoshioka, K. *et al.* Ca^{2+}-induced, Rho- and Rho kinase-dependent regulation of myosin phosphatase and contraction in isolated vascular smooth muscle cells. *Mol. Pharmacol.* **71**, 912–920 (2007).
21. Traer, C.J. *et al.* Are class II phosphoinositide 3-kinases potential targets for anticancer therapies? *Bull. Cancer* **93**, E53–E58 (2006).
22. Gaidarov, I. *et al.* Individual phosphoinositide 3-kinase C2α domain activities independently regulate clathrin function. *J. Biol. Chem.* **280**, 40766–40772 (2005).
23. Falasca, M. & Maffucci, T. Role of class II phosphoinositide 3-kinase in cell signalling. *Biochem. Soc. Trans.* **35**, 211–214 (2007).
24. Wang, Y. *et al.* Class II phosphoinositide 3-kinase α-isoform regulates Rho, myosin phosphatase and contraction in vascular smooth muscle. *Biochem. J.* **394**, 581–592 (2006).
25. Harris, D.P. *et al.* Requirement for class II phosphoinositide 3-kinase C2α in maintenance of glomerular structure and function. *Mol. Cell. Biol.* **31**, 63–80 (2011).
26. Moses, K.A. *et al.* Embryonic expression of an Nkx2–5/Cre gene using ROSA26 reporter mice. *Genesis* **31**, 176–180 (2001).
27. Kisanuki, Y.Y. *et al.* Tie2-Cre transgenic mice: a new model for endothelial cell-lineage analysis *in vivo*. *Dev. Biol.* **230**, 230–242 (2001).
28. Wang, Y. *et al.* Ephrin-B2 controls VEGF-induced angiogenesis and lymphangiogenesis. *Nature* **465**, 483–486 (2010).
29. Pannekoek, W.J. *et al.* Cell-cell junction formation: the role of Rap1 and Rap1 guanine nucleotide exchange factors. *Biochim. Biophys. Acta* **1788**, 790–796 (2009).
30. Gillooly, D.J. *et al.* Localization of phosphatidylinositol 3-phosphate in yeast and mammalian cells. *EMBO J.* **19**, 4577–4588 (2000).
31. Lindmo, K. & Stenmark, H. Regulation of membrane traffic by phosphoinositide 3-kinase. *J. Cell Sci.* **119**, 605–614 (2006).
32. Di Paolo, G. & De Camilli, P. Phosphoinositides in cell regulation and membrane dynamics. *Nature* **443**, 651–657 (2006).
33. Bryan, B.A. *et al.* RhoA/ROCK signaling is essential for multiple aspects of VEGF-mediated angiogenesis. *FASEB J.* **24**, 3186–3196 (2010).
34. Macia, E. *et al.* Dynasore, a cell-permeable inhibitor of dynamin. *Dev. Cell* **10**, 839–850 (2006).
35. Cauwels, A. *et al.* Anaphylactic shock depends on PI3K and eNOS-derived NO. *J. Clin. Invest.* **116**, 2244–2251 (2006).
36. Daugherty, A. & Cassis, L.A. Mouse models of abdominal aortic aneurysms. *Arterioscler. Thromb. Vasc. Biol.* **24**, 429–434 (2004).
37. Di Gennaro, A. *et al.* Increased expression of leukotriene C4 synthase and predominant formation of cysteinyl-leukotrienes in human abdominal aortic aneurysm. *Proc. Natl. Acad. Sci. USA* **107**, 21093–21097 (2010).
38. Wheeler, M. & Domin, J. The N-terminus of phosphoinositide 3-kinase-C2β regulates lipid kinase activity and binding to clathrin. *J. Cell. Physiol.* **206**, 586–593 (2006).
39. Simonsen, A. & Tooze, S.A. Coordination of membrane events during autophagy by multiple class III PI3-kinase complexes. *J. Cell Biol.* **186**, 773–782 (2009).
40. Johnson, E.E. *et al.* Gene silencing reveals a specific function of hVps34 phosphatidylinositol 3-kinase in late versus early endosomes. *J. Cell Sci.* **119**, 1219–1232 (2006).
41. Doherty, G.J. & McMahon, H.T. Mechanisms of endocytosis. *Annu. Rev. Biochem.* **78**, 31.1–31.46 (2009).
42. Zoncu, R. *et al.* A phosphoinositide switch controls the maturation and signaling properties of APPL endosomes. *Cell* **136**, 1110–1121 (2009).
43. Palamidessi, A. *et al.* Endocytic trafficking of Rac is required for the spatial restriction of signaling in cell migration. *Cell* **134**, 135–147 (2008).
44. van Nieuw Amerongen, G.P. *et al.* Involvement of Rho kinase in endothelial barrier maintenance. *Arterioscler. Thromb. Vasc. Biol.* **27**, 2332–2339 (2007).
45. Yamada, S. & Nelson, W.J. Localized zones of Rho and Rac activities drive initiation and expansion of epithelial cell-cell adhesion. *J. Cell Biol.* **178**, 517–527 (2007).
46. Harris, T.J.C. & Tepass, U. Adherens junctions: from molecules to morphogenesis. *Nat. Rev. Mol. Cell Biol.* **11**, 502–514 (2010).
47. Abraham, S. *et al.* VE-cadherin–mediated cell-cell interaction suppresses sprouting via signaling to MLC2 phosphorylation. *Curr. Biol.* **19**, 668–674 (2009).
48. Noda, K. *et al.* Vascular endothelial-cadherin stabilizes at cell-cell junctions by anchoring to circumferential actin bundles through α- and β-catenins in cyclic AMP-Epac-Rap1 signal-activated endothelial cells. *Mol. Biol. Cell* **21**, 584–596 (2010).
49. Webb, D.J., Parsons, J.T. & Horwits, A.F. Adhesion assembly, disassembly and turnover in migrating cells—over and over and over again. *Nat. Cell Biol.* **4**, E97–E100 (2002).
50. Mitra, S.K., Hanson, D.A. & Schlaepfer, D.D. Focal adhesion kinase: in command and control of cell motility. *Nat. Rev. Mol. Cell Biol* **6**, 56–68 (2005).
51. Shivas, J.M. *et al.* Polarity and endocytosis: reciprocal regulation. *Trends Cell Biol.* **20**, 445–452 (2010).

ONLINE METHODS

Mice. All mice used in this study were bred and maintained at the Institute for Experimental Animals, Advanced Science Research Center, Kanazawa University under specific pathogen–free conditions. All procedures were conducted in accordance with the Fundamental Guidelines for Proper Conduct of Animal Experiment and Related Activities in Academic Research Institutions under the jurisdiction of the Ministry of Education, Culture, Sports, Science and Technology of Japan and approved by the Committee on Animal Experimentation of Kanazawa University.

A gene-targeting strategy to generate global *Pik3c2a*-null mice is described in the **Supplementary Methods**. Four lines of *Cre* mice, *Tie2*-Cre (ref. 27), *SM22a*-Cre (B6.129S6-*Tagln*$^{tm2(Cre)Yec}$/J, Jackson Lab), *Nkx2-5*–Cre (ref. 26) and tamoxifen-inducible endothelial-cell–specific *Cdh5*(PAC)-CreER^{T2} (refs. 28,52,53), were bred with *Pik3c2a*$^{flox/+}$ or *Pik3c2a*$^{flox/flox}$ mice to generate *Pik3c2a*$^{\Delta EC}$ (*Pik3c2a*$^{flox/flox}$; *Tie2*-Cre), *Pik3c2a*$^{\Delta SMC}$ (*Pik3c2a*$^{flox/flox}$; *SM22a*-Cre), *Pik3c2a*$^{\Delta MC}$ (*Pik3c2a*$^{flox/flox}$; *Nkx2-5*–Cre) and *Pik3c2a*$^{i\Delta EC}$ (*Pik3c2a*$^{flox/flox}$; *Cdh5*(PAC)-CreER^{T2}) mice, respectively. Cre-negative littermates were used as controls. To verify the efficiency of Cre recombination, Cre mice were mated with mice from the *Cre* reporter transgenic line *ROSA26*-LacZ (B6.129S4-*Gt(ROSA)26Sor*^{tm1Sor}/J, Jackson Lab). All mice had a C57BL/6J genetic background. Gene inactivation in pups was triggered by i.p. injection of 50 μl of tamoxifen solution (Sigma, T5648; 10 mg ml^{-1} corn oil) once at P3 or P6. The phenotypes of the mutant mice were analyzed at P6 or P9, as indicated. For adult mice, tamoxifen was administered by i.p. injection of 100 μl of a 10 mg ml^{-1} tamoxifen stock solution (that is, 1 mg per injection) a total of seven times, every second day.

Cell culture and siRNA knockdown. Mouse embryonic fibroblasts (MEF) and MASM were isolated from *Pik3c2a*$^{flox/flox}$ mice and used for *in vitro* assays. *Pik3c2a*$^{flox/flox}$ MEF and MASM cells were cultured in DMEM (WAKO) and advanced DMEM (Invitrogen) supplemented with 10% FBS, respectively. The cells were cultured to 70% confluency and then were infected with adenovirus encoding Cre recombinase (AdCre) in the absence of serum. Infection with adenovirus encoding LacZ (AdLacZ) was used as control. After 1 h, culture medium containing 10% FBS was added, and the cells were allowed to recover for the next 48 h. Greater than 90% C2α deletion was confirmed by western blotting (**Supplementary Fig. 13d**). HUVEC (passage 2–4) (Lonza) were grown in endothelial basal medium supplemented with 2% FBS and growth factor supplement cocktail (complete growth medium) (EBM2, Lonza, CC-3162). HUVEC were transfected with 20 nM of siRNA using Lipofectamine 2000 (Invitrogen) in OptiMEM (2 μl ml^{-1}; Gibco) according to the manufacturer's instructions. After 4 h, the culture medium was replaced with complete growth medium. The cells were cultured for a further 48–72 h before processing for immunofluorescence staining and other assays. The target sequences of the siRNA used are listed in the **Supplementary Methods**.

Whole-mount staining and immunofluorescence staining. For tissue immunohistochemistry, 4% paraformaldehyde (PFA)-fixed, paraffin-embedded tissue sections were stained using standard methods. Frozen sections were prepared by cryoprotecting fixed tissue in 20% sucrose overnight at 4 °C, snap freezing the tissue in optimal cutting temperature compound (Tissue Tek) and sectioning the tissue with a Sakura Tissue-Tek Cryo$_3$ Cryostat. Sections (7–30 μm) were washed in Ca^{2+}- and Mg^{2+}-free Dulbecco's PBS and incubated with primary antibodies diluted in the antibody dilution solution (Can Get Signal, Toyobo) overnight at 4 °C or for 2 h at room temperature. Sections were then washed in PBS with 0.1% Triton X-100 and incubated with Alexa Flour–conjugated secondary antibodies for 1 h at room temperature. The antibodies used are listed in the **Supplementary Methods**. Whole-mount immunostaining of CD31 was performed using the labeled streptavidin biotin method, as described previously[54]. Alternatively, skin from the embryo head region, flat-mount retinas from postnatal mice (P6 or P9) and en face preparations of mouse aorta were used for whole-mount immunostaining, as described previously[55] with minor modifications. PFA-fixed tissues were permeabilized with methanol when necessary. Samples were incubated in blocking buffer (1% BSA and 0.3% Triton X-100 in PBS) for 2 h and washed three times in Pblec buffer (1% Triton X-100, 1 mM $CaCl_2$, 1 mM $MgCl_2$ and 1 mM $MnCl_2$ in PBS, pH 6.8). For immunofluorescence staning, samples were incubated overnight at 4 °C with gentle rocking with antibodies to biotinylated isolectin B4 (Vector B-1205, 1:50), CD31 (1:100, BD, 557355), FITC-conjugated α-SMA (1:100, Sigma, A2647), NG2 (1:100, Chemicon, ab5320) or biotinylated VE-cadherin (1:100, eBoscience 13-1441); the antibodies were diluted in Pblec buffer (1% Triton X-100, 1 mM $CaCl_2$, 1 mM $MgCl_2$ and 1 mM $MnCl_2$ in PBS, pH 6.8). For detection using secondary antibodies, Alexa Fluor-594–conjugated streptavidin (1:200, Molecular Probe, S-11227) or Alexa Fluor-488–conjugated species-specific IgG antibodies (1:500, Molecular Probe; anti-mouse IgG (H+L), A11001; anti-rabbit IgG (H+L), A11008; anti-rat IgG (H+L), A11006) diluted in blocking buffer were applied overnight at 4 °C. The vascular area in skin or retina, number of branch points and filopodial bursts in arterial zones per unit area in flat-mount retina were measured or counted from randomly defined 15–20 microscopic fields from 5–8 retinas per group for each genotype. CD31-positive vascular areas in skin and retinas were quantified using ImageJ software. Values were normalized with field sizes.

For immunofluorescence cell staining, cells were cultured on collagen-I (Type I-P, Nitta Gelatin)-coated glass-bottom dishes or Lab-Tek chamber slides in a complete growth medium (see below) and allowed to adhere overnight. The cells were rinsed with prewarmed Ca^{2+}- and Mg^{2+}-containing PBS once and fixed in prewarmed 4% fresh PFA or PBS for 15 min, washed in PBS and then permeabilized in 0.2% Triton X-100 in PBS for 5 min when necessary. The cells were incubated with blocking reagent (DAKO, X0909) for 10 min to inhibit nonspecific protein binding. For some experiments, the cells were alternatively fixed and permeabilized by immersion in acetone or methanol at −20 °C for 10 min. After blocking, cells were incubated with primary antibodies for 2 h at room temperature or overnight at 4 °C or with Alexa Fluor-594–conjugated phalloidin (1:200, Molecular Probe, A-12381). The cells were then incubated for 1 h with goat Alexa Flour-488–(1:1,1000, Molecular Probe, A-11029) or -594–conjugated secondary antibodies (1:1,000, Molecular Probe, A-11032) in PBS. For immunostaining of active GTP-RhoA, HUVEC were serum starved in M199 medium including 0.5% fatty-acid–free BSA overnight and were stimulated with VEGF-A_{165} (30 ng ml^{-1}, PeproTech) or EBM2 complete growth medium for 30 min; the cells were then stained with antibody specific for active RhoA (GTP-RhoA; NewEast Biosciences, 26904, 1:400) (this antibody was generated using GTPγS-bound RhoA antigen) and Alexa Fluor-594–conjugated phalloidin (for F-actin staining) as described above. Where appropriate, cells were counterstained with DAPI (Molecular Probe, 300 nM) for 5 min. The cells were mounted on Prolong Gold (Molecular Probe) as an antiphotobleaching agent and examined using an inverted fluorescence microscope (Olympus IX70) under a PlanApo ×40/NA0.95 objective or a confocal laser-scanning microscope (Zeiss Axiovert 200M with LSM5 Pascal) equipped with a PlanApo ×63/NA1.4 oil-immersion objective. For quantification, the positive area in stained images was calculated using ImageJ software. Quantification was carried out for at least three independent experiments with >50 cells per experiment. Adobe Photoshop was used to adjust image levels and process image overlays.

Detection of LacZ by X-gal staining and immunostaining. For 5-bromo-4-chloro-3-indolyl-β-D-galactoside (X-gal) staining, whole embryos or tissues were dissected from E16.5–E18.5 embryos, fixed in X-gal fixative solution (0.25% glutaraldehyde, 5 mM ethylene glycol tetraacetic acid (EGTA) and 2 mM $MgCl_2$ in PBS) at room temperature for 30 min and then washed in wash buffer (2 mM $MgCl_2$ and 0.02% NP-40 in PBS) for 10 min (three times). Samples were stained in X-gal staining solution (1 mg ml^{-1} X-gal, 5 mM potassium ferricyanide and 5 mM potassium ferrocyanide in wash buffer) at 37 °C until the desired staining level was achieved. Alternatively, LacZ-specific antibody (1:400, MP Cappel, 59761) was used for multicolor immunofluorescence staining, as described previously[56]. Samples were imaged on a Leica MZ16F stereomicroscope (whole-mount tissue) or a Zeiss Axiovert 200M microscopy with a LSM5 Pascal confocal laser-scanning unit using Image Browser software (Carl Zeiss).

Postnatal retinal angiogenesis model. Eyes were dissected from neonatal mice (mutants or their respective control littermates) and fixed in 4% PFA for 2 h at room temperature. Flat-mount isolectin B4 staining of retinas was performed as described in the 'whole-mount staining' section above. The spreading of the retinal vasculature along the vitreal surface was quantified by flat mounting the retina and analysis using ImageJ software. The number of branch points and

filopodial bursts in arterial zones per unit area in the flat-mount retina was counted from 15–20 randomly defined microscopic fields from 5–8 retinas per group for each genotype. The values were normalized by field size. For labeling of proliferating cells in the retina, 300 μg of BrdU (BD) in 100 μl PBS per pup was i.p. injected 2 h before euthanasia. After isolectin B4 staining, retinas were stained with BrdU-specific antibody (1:100, BD, 555627).

Postischemic hindlimb angiogenesis model. Male *Pik3c2a*$^{i\Delta EC}$ mice and control *Pik3c2a*$^{flox/flox}$ littermates (C57BL/6 background) were subjected to surgical procedures to achieve unilateral hindlimb ischemia, as described previously[57]. In brief, the femoral artery was exposed and ligated with 8-0 silk, and the whole length of the femoral artery was excised. The blood flow of the ischemic (left) and contralateral nonischemic (right) hindlimbs was measured with a laser Doppler blood flow (LDBF) analyzer (Moor Instruments) before and after operation. The stored data were analyzed to quantify the mean LDBF per unit of two-dimensional area on the en face image of each entire hindlimb in mice in the supine position, which was determined using software provided by the manufacturer (Moor Instruments). For each mouse, results were expressed as the ratio of the LDBF value in the ischemic (left) limb to the value in the nonischemic control (right) limb at a given time point.

Tumor angiogenesis model. LLC cells (1×10^6) or B16-BL6 melanoma cells (5×10^5) were subcutaneously implanted in the dorsal backs of 8- to 10-week-old male *Pik3c2a*$^{i\Delta EC}$ mice and control *Pik3c2a*$^{flox/flox}$ littermates (C57BL/6 background)[58]. Tumor volumes were calculated by the formula $V = (LW^2)/2$, where L and W denote the longer and shorter diameter, respectively.

PAF-induced anaphylaxis model. To trigger anaphylactic shock, 10- to 12-week-old male *Pik3c2a*$^{+/-}$ or littermate wild-type mice received i.v. injection of PAF (12 μg per kg body weight or 20 μg per kg body weight in 100 μl saline) in the tail vein, and their survival was followed. In separate mice, 15 min after infusion, blood samples were obtained from the right ventricle to determine hematocrit content. To assess vascular leakage in the lung, 100 μl of a 1% solution of Evans blue dye in saline was injected into the tail vein together with PAF. Fifteen minutes later, mice were perfused with saline in the right ventricle to remove the intravascular Evans blue dye. The lungs were excised and extracted in 1 ml of formamide at 55 °C overnight. Evans blue content was determined by the equation: corrected 620-nm optical density (OD_{620} (Evans blue) − (1.426 × OD_{740} (hemoglobin) + 0.03).

Ang II infusion aortic aneurysm model. An osmotic minipump (Alzet, model 1002) containing Ang II (Calbiochem, 1.0 mg per kg body weight per day) was implanted in the midscapular region in male *Pik3c2a*$^{+/-}$ or *Pik3c2a*$^{i\Delta EC}$ and wild-type littermates. Mice were euthanized at day 14 after minipump implantation, and aortic tissue was removed. Aneurysm severity was graded according to the following criteria[59]: grade 1, remodeled tissue in the suprarenal region frequently containing thrombus; grade 2, pronounced bulbous form of grade 1 containing thrombus; grade 3, multiple aneurysms containing thrombus; or ruptured, ruptured aortic aneurysm. Both cryostat and paraffin-embedded aortic sections were used for the characterization of aneurysmal lesions. Elastin was visualized using Elastica van Gieson staining. Fibrosis was evaluated using Azan staining. Infiltrating macrophages were detected using Mac-3–specific antibody (1:400, BD, 553322) immunostaining. Miles assay and gelatin zymography were performed as described below.

Live-cell imaging and FRET analysis. Cells transfected with expression vectors for GFP-C2α, GFP- or mRFP-2 × FYVE and VE-cadherin–GFP or –mRFP were plated on collagen-coated glass-bottomed dishes (MatTek, P35G-1.5-20-C) or LabTek chamber slides (Thermo Scientific, 177402) and allowed to adhere for 16 h before imaging. Cells on a heated stage (37 °C; Tokai-Hit) were observed under a custom confocal microscope based on an inverted IX70 microscope (Olympus) equipped with an UPLSAPO ×60/NA1.35-oil or ×40/0.95-oil objective, a confocal laser unit (CSU10, Yokogawa), an electron multiplying charge-coupled device (EMCCD) digital camera (iXon, Andor) and a Light engine (Lumencor, Inc) for three-dimensional time-lapse confocal imaging at a rate of two frames per second. The acquisition and process were controlled by iQ software (Andor).

For FRET analysis, HUVEC were transfected with the pRaichu-RhoA FRET probe vector (provided by M. Matsuda at Kyoto University) using an Amaxa Nucleofector system (Lonza) and imaged using a custom confocal microscope system configured with a CFP and YFP filter set (Di01-T445/515/561-13 × 15 × 0.5, Semrock). Pseudograyscale ratio images were generated from images from the CFP and FRET channels using Andor iQ software.

Cell proliferation, migration, adhesion, apoptosis and tube-formation assay. Cell proliferation was analyzed using an MTS (3-(4,5-dimethylthiazol-2-yl)-5-(3-carboxymethoxyphenyl)-2-(4-sulfophenyl)-2H-tetrazolium, inner salt) assay kit (Promega) according to the manufacturer's instructions. For the modified Boyden chamber cell migration assay, siRNA-transfected HUVEC (5×10^4 cells per well) resuspended in M199 medium (Gibco) containing 0.25% fatty-acid–free BSA (Sigma-Aldrich) or adenovirus-infected MASM cells (2×10^4 cells per well) resuspended in serum-free DMEM were placed in the upper chamber and allowed to migrate across collagen type I–coated polycarbonate filters (8-μm pore size, Neuro Probe) for 6 h toward the lower chamber with or without VEGF-A (0.5–100 ng ml^{-1}) for HUVEC and with or without PDGF-BB (0.1–30 ng ml^{-1}) for MASM. The cells remaining on the upper surface of the transwell membranes were removed, and the cells that had migrated to the lower surface were methanol fixed, stained with Diff-Quick (Sysmex) and counted in five random microscopic fields. To analyze cell adhesion to a collagen-covered surface, HUVEC that had been transfected with scrambled (control) or C2α-siRNAs were seeded onto 96-well tissue culture plates coated with collagen type I and incubated in the presence of VEGF-A (30 ng ml^{-1}) for the indicated time periods. After washing with PBS three times to remove nonadherent cells, adherent cells were stained with Diff-Quick and quantified in triplicates with a microplate reader (Bio-Rad). To assay apoptosis, cells were immunostained with cleaved caspase-3–specific antibody (1:1,000, Cell Signaling, 9664) according to the manufacturer's instructions (Cell Signaling). To assay tube formation, siRNA-transfected HUVEC (2.5×10^4 cells) in EBM2 containing 2% FBS with or without supplements were seeded onto 200 μl of growth-factor–reduced Matrigel in a 24-well plate in the absence or presence of VEGF-A (30 ng ml^{-1}) and incubated for 12–16 h. Tube formation was quantified after 12–16 h by measuring the cumulative tube length and number of branching points in five random microscopic fields using ImageJ (NIH).

Pulldown assay of small G protein activity. The pulldown assays for GTP-bound RhoA, Rac1 and Rap1 were performed as described previously[60]. In brief, confluent HUVEC were stimulated and lysed with either Rho extraction buffer (50 mM Tris-HCl, pH 7.5, 500 mM NaCl, 10 mM $MgCl_2$, 1% Triton X-100, 0.5% sodium deoxycholate, 0.1% SDS, 10% glycerol and protease and phosphatase inhibitor cocktail (Roche)), Rac extraction buffer (50 mM Tris-HCl, pH 7.5, 500 mM NaCl, 10 mM $MgCl_2$, 1% Triton X-100, 0.5% sodium deoxycholate, 0.1% SDS, 10% glycerol and protease inhibitor cocktail) or Rap extraction buffer (20 mM Tris-HCl, pH 7.5, 100 mM NaCl, 10 mM $MgCl_2$, 1% NP-40, 1 mM EGTA and protease inhibitor cocktail). The lysates were cleared by centrifugation, and the resultant supernatants were incubated for 60 min at 4 °C with glutathione-Sepharose 4B beads coupled to the Rho binding domain of Rhotekin for RhoA, the PAK1-CRIB domain for Rac1 or the Rap-binding domain of Ral-GDI for Rap1. The beads were washed and bound proteins were solubilized by the addition of 30 μl of SDS-PAGE 2 × Laemmli's loading buffer, followed by separation on 15% SDS-PAGE gels and western blotting with RhoA-specific (1:1,000, Santa Cruz sc-418, 26C4), Rac1-specific (1:2,000, Millipore 05-389, 23A8) and Rap1-specific (1:1,000, BD, 610195) antibodies, respectively.

***In vitro* transwell and *in vivo* Miles permeability assay.** HUVEC transfected with C2α-siRNA or sc-siRNA were seeded onto collagen-coated transwells with a 0.4-μm pore size (Costar) and allowed to form a monolayer. Permeability was stimulated with VEGF-A_{165} (50 ng ml^{-1}) or thrombin (0.5 U ml^{-1}) for 30 min, followed by the addition of FITC-dextran (at a final concentration of 1 mg ml^{-1}) (molecular mass (Mr) = 42 kDa; Sigma-Aldrich) into the top chamber followed by incubation for an additional 30 min. The amount of FITC-dextran in the bottom chamber was determined by fluorometric analysis.

To assay *in vivo* permeability, 1.0% Evans blue dye in saline (100 μl) was i.v. injected into the tail vein of *Pik3c2a*$^{+/+}$ and *Pik3c2a*$^{+/-}$ mice and allowed to